Mathematical Modelling of Natural Phenomena
Math. Model. Nat. Phenom. www.mmnp-journal.org
https://doi.org/10.1051/mmnp/ (will be inserted later)

ANALYTICAL DETECTION OF STATIONARY TURING PATTERN IN A PREDATOR-PREY SYSTEM WITH GENERALIST PREDATOR

Subrata Dey[1], Malay Banerjee[1] and S Ghorai [1,*]

Abstract. A prey-predator model with prey dependent Holling type-II functional response and a generalist predator exhibits complex dynamics in response to parameter variation. Generalist predators implicitly exploiting multiple food resources reduce predation pressure on their focal prey species that causes it to become more stable compared to a prey-predator system with specialist predator. In the temporal system, bistability and tristability are observed along with various global and local bifurcations. Existence of homogeneous and heterogeneous positive steady state solutions are shown to exist for suitable ranges of parameter values in the spatio-temporal diffusive system. Weakly nonlinear analysis using multi-scale perturbation technique is employed to derive amplitude equation for the stationary patterns near the Turing bifurcation threshold. The analytical results of the amplitude equations are validated using numerical simulations. We also identify bifurcation of multiple stable stationary patch solutions as well as dynamic pattern solution for parameter values in the Turing and Turing-Hopf regions.

Mathematics Subject Classification. — Please, give AMS classification codes —.

...

1. Introduction

Mathematical modeling plays a significant role in understanding various complex ecological phenomena. In this context, prey-predator intra- and inter-species interactions are commonly used to formulate various temporal and spatio-temporal models following the pioneering work of Lotka [1] and Volterra [2]. Spatial component in the form of diffusion is introduced in a temporal model to mimic the random movement of individuals leading to reaction-diffusion (RD) equations. In a seminal paper [3], Turing showed that the concentrations of two chemical species of different diffusion rates transformed from a nearly spatially homogeneous initial state to a spatially heterogeneous stationary pattern. Segel and Jackson [4] first used Turing's model to explain the spatial pattern formation in ecological systems. At the same time, Gierer and Meinhardt [5] justified Turing's RD model formulation and studied its properties using numerical simulation. Further, the RD models have been widely used by other researchers to explain pattern formulation in fish skin [6], terrestrial vegetation [7, 8], plankton patchiness [9, 10], ecological invasion [11, 12], spread of epidemics [13, 14], etc. In this regard, RD system to formulate spatio-temporal population interaction [15, 16] is an important tool to study the spatial impact on the temporal dynamics when the population are heterogeneously distributed in their habitat. Gause [17] first showed

Keywords and phrases. Hopf bifurcation; Global bifurcation; Turing instability; Amplitude equation; Spatial pattern

[1] Department of Mathematics and Statistics, Indian Institute of Technology Kanpur, Kanpur 208016, Uttar Pradesh, India.
*Corresponding author: sghorai@iitk.ac.in

Published by EDP Sciences and available at https://www.mmnp-journal.org or https://doi.org/10.1051/mmnp/2022032

the significance of spatial heterogeneity in long term survival of species *paramecium* and *didinium* through a laboratory experiment. Experimenting on two mite species, *Typhlodromus occidentalis* and *Eotetranychus sexmaculatus*, Huffaker [18] observed that both species can survive for long time in appropriate heterogeneous environment whereas homogeneous environment set up can lead to extinction of both species.

Turing and Turing-Hopf bifurcations play significant roles in the emergence of various spatio-temporal patterns [19–21]. Spatio-temporal patterns can be classified in two categories: stationary patterns and dynamic patterns. Turing bifurcation is responsible for the formation of stationary heterogeneous patterns through Turing instability which occurs when a temporally stable homogeneous solution becomes unstable due to small amplitude of spatially heterogeneous perturbation and the resulting patterns are known as Turing patterns [3, 4, 22]. These patterns may resemble like spots (hot and cold), stripes or a mixture of them [23–25]. Most of the previous works mainly focused on the dependence of Turing pattern formation on control parameter(s) of the RD system [20,21,24]. However, very little attention has been paid on the mode selection problem of the Turing patterns [26–28]. Dynamic spatial patterns, which are usually observed in Turing-Hopf domain [21, 29, 30], are characterized by periodic, quasi-periodic or even spatio-temporal chaotic patterns with the advancement of time. Apart from these, dynamic spatially heterogeneous patterns are also observed in RD systems due to other mechanisms that include travelling wave, periodic travelling wave, modulated travelling wave and invasion [12, 31–33].

Predator-prey models for two species interaction are building blocks for several food-chains and food-webs. In such models, predators can be categorized into two groups, namely, specialist predators and generalist predators. Specialist predators become extinct in absence of prey since it completely depends on prey species for food. In the prey-predator system with specialist predator, persistence of both species is observed in a small range of parameter values and the system is driven to extinction outside the parameter range due to the disappearance of co-existing steady state from the interior of first quadrant. Generalist predators are diverse and abundant and they have significant role in natural systems. Generalist predators can survive in absence of their focal prey as they have alternative food sources other than its focal prey. Compared to the specialist predators, generalist predators have received less attention. Spencer and Collie [34] added a linear growth term with the quadratic death rate in generalist predator population so that they have logistic growth law for the predator in the absence of prey population. Alternative food sources of the generalist predator may include a variety of prey sources which can be modelled by two or more prey population along with the predator population [35]. Classical RD prey-predator models with specialist predator having linear death rate and prey's density dependent numerical response are unable to produce stationary patterns [29, 36]. But consideration of intra-species competition among predators in the same model supports the formation of Turing patterns [9,37]. In addition, prey-predator models with linear death rate of specialist predator and predator's density dependent functional response can support Turing pattern formation too [21,38]. Liao et al. [39] studied the effect of diffusion in a ratio-dependent prey-predator model with generalist predator.

In this work, we have chosen a generalist predator with logistic growth rate and prey-predator interaction is modelled with prey dependent functional response. We first carry out a complete bifurcation analysis of the temporal model and illustrate some representative dynamics for certain range of parameter values. Existence of homogeneous and heterogeneous positive steady state solutions are established for suitable ranges of parameter values in the RD system. Analytical expressions of Turing patterns corresponding to unstable eigen modes near the mode selecting Turing thresholds are derived using weakly nonlinear analysis and these are validated with the help of numerical simulations.

This paper is organized as follows. In section 2, we describe our temporal system, existence of its equilibrium points and their stability, followed by section 3 that analyzes all possible local bifurcations and a parametric bifurcation diagram in section 4. Next, we consider the corresponding one dimensional spatial extension and prove the existence of global solution and stationary coexistence solution in section 5. We also check the stability of the homogeneous steady state, derive the Turing instability criteria and various mode selecting thresholds for parameter values in the Turing domain. Amplitude equation is derived using weakly nonlinear analysis in

section 6 and the results of the weakly nonlinear analysis are compared with the numerical results in section 7. Finally, discussions and conclusions are drawn in section 8.

2. Temporal Model

We consider a prey-predator model with generalist predator where both the species have intra-specific competition and their interaction is modelled by Holling type-II functional response. Let $N(T)$ and $P(T)$ be the prey and predator population density at time T respectively. The system is governed by two ordinary differential equations

$$\frac{dN}{dT} = r_1 N - b_1 N^2 - \frac{mNP}{1+mhN}, \tag{2.1a}$$

$$\frac{dP}{dT} = r_2 P - b_2 P^2 + \frac{emNP}{1+mhN}, \tag{2.1b}$$

subject to initial conditions $N(0), P(0) \geq 0$. Parameters r_1, r_2 represent the intrinsic growth rates of the prey and predator population respectively and b_1, b_2 are the corresponding intra-species competition. The parameter m represents the consumption rate of prey by the predator and h is the handling time, i.e., the average time spent by predator to capture a prey. Also, e is the conversion coefficient which represents the fraction of consumed prey helping to the predator growth. All the parameters in the system (2.1) are assumed to be positive.

We take $t = r_1 T, u = b_1 N/r_1$ and $v = b_2 P/r_2$ for dimensionless time, prey population density and predator population density respectively. Using these variables in system (2.1), we obtain

$$\frac{du}{dt} = u(1-u) - \frac{auv}{\alpha+u} \equiv F_1(u,v) = uf_1(u,v), \tag{2.2a}$$

$$\frac{dv}{dt} = \eta v(1-v) + \frac{buv}{\alpha+u} \equiv F_2(u,v) = vf_2(u,v), \tag{2.2b}$$

where

$$f_1(u,v) = 1 - u - \frac{av}{\alpha+u} \tag{2.3a}$$

and

$$f_2(u,v) = \eta(1-v) + \frac{bu}{\alpha+u}. \tag{2.3b}$$

Here, $a = b_1 r_2/b_2 r_1^2 h, \alpha = b_1/mhr_1, \eta = r_2/r_1$ and $b = eb_1 r_2/b_2 r_1^2 h$ are positive dimensionless parameters.

2.1. Positivity and boundedness

Any solution $(u(t), v(t))$ of system (2.2), starting from a non-negative initial condition $(u(0), v(0))$, remains positive and bounded for all time t. Proof of positivity and boundedness are presented in Appendix A.

2.2. Equilibrium points and their existence

The system (2.2) always has trivial equilibrium $E_0(0,0)$, and two axial equilibria $E_1(1,0)$ and $E_2(0,1)$. Intersection of non-trivial prey nullcline $f_1(u,v) = 0$ and predator nullcline $f_2(u,v) = 0$ in the first quadrant generates co-existing equilibrium points $E_j^*(u_j, v_j)$, where j can vary from 1 to 3.

The first component u_j of E_j^* is a root of the cubic equation

$$G(u) \equiv u^3 + a_2 u^2 + a_1 u + a_0 = 0, \tag{2.4}$$

where $a_2 = (2\alpha - 1), a_1 = (\alpha^2 - 2\alpha + a + ab/\eta)$ and $a_0 = \alpha(a - \alpha)$. The corresponding v_j is given by

$$v_j = \frac{(1-u_j)(\alpha+u_j)}{a}. \tag{2.5}$$

The number of co-existing equilibrium points depends on three parametric conditions for α described below:

I. For $\alpha > \alpha_{CP_1}$, the system (2.2) has only one co-existing equilibrium point [see Fig. 1(a)].
II. For $a < \alpha < \alpha_{CP_1}$, we have three subcases: (a) $\eta_{SN_I} < \eta < \eta_{SN_{II}}$; or (b) $0 < \eta < \eta_{SN_I}$; or (c) $\eta > \eta_{SN_{II}}$. In the first subcase, the system has three co-existing equilibrium points [see Fig. 1(b)] and only one equilibrium point in the second subcase [see Fig. 1(c)] and third subcase [see Fig. 1(d)].
III. For $\alpha < a$, we have two sub-cases: (a) $\eta < \eta_{SN_I}$; or (b) $\eta > \eta_{SN_I}$. In the first subcase, no interior equilibrium point exists [see Fig. 1(e)] and two interior equilibria exist in the second subcase [see Fig. 1(f)].

The values $\eta_{SN_I}, \eta_{SN_{II}}$ of η and α_{CP_1} of α are various bifurcation threshold values that we will describe later.

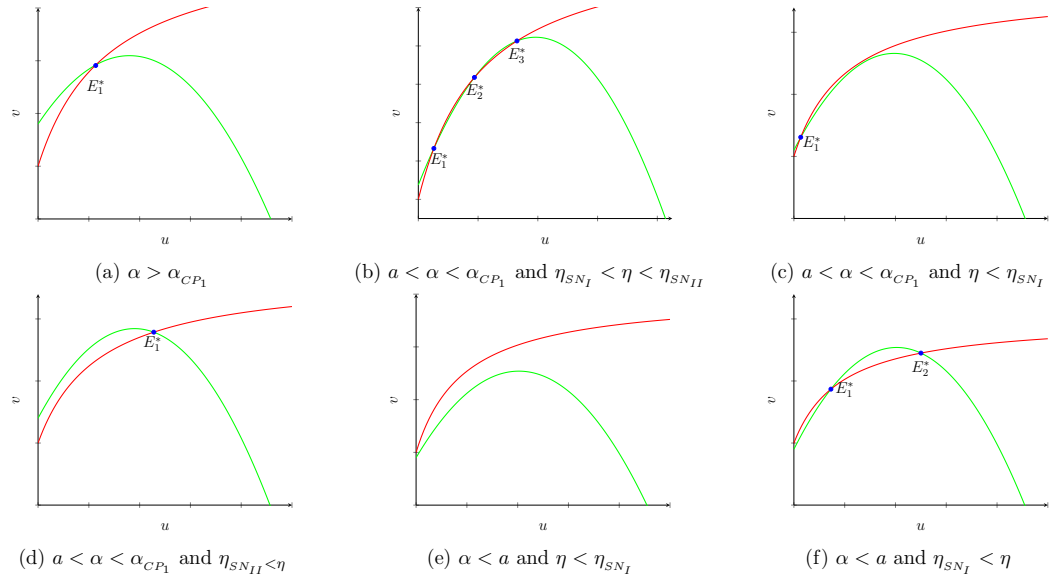

(a) $\alpha > \alpha_{CP_1}$ (b) $a < \alpha < \alpha_{CP_1}$ and $\eta_{SN_I} < \eta < \eta_{SN_{II}}$ (c) $a < \alpha < \alpha_{CP_1}$ and $\eta < \eta_{SN_I}$

(d) $a < \alpha < \alpha_{CP_1}$ and $\eta_{SN_{II}} < \eta$ (e) $\alpha < a$ and $\eta < \eta_{SN_I}$ (f) $\alpha < a$ and $\eta_{SN_I} < \eta$

FIGURE 1. Location of the co-existing equilibrium points for different configurations of the nontrivial nullclines depending on parametric conditions. Here red and green color curves represent the nontrivial predator and prey nullclines respectively.

2.3. **Linear stability of equilibria**

To find the linear stability of an equilibrium point $E^*(u^*, v^*)$, we linearize the system (2.2) about the equilibrium point. This leads to the Jacobian matrix of the system (2.2) evaluated at $E^*(u^*, v^*)$ given by

$$J(E^*) = \begin{bmatrix} 1 - 2u^* - \frac{av^*}{(u^*+\alpha)} + \frac{au^*v^*}{(u^*+\alpha)^2} & -\frac{au^*}{(u^*+\alpha)} \\ \frac{bv^*}{(u^*+\alpha)} - \frac{bu^*v^*}{(u^*+\alpha)^2} & \eta(1-2v^*) + \frac{bu^*}{(u^*+\alpha)} \end{bmatrix} \equiv \begin{bmatrix} a_{10} & a_{01} \\ b_{10} & b_{01} \end{bmatrix}. \tag{2.6}$$

The equilibrium point E^* is stable (resp. unstable) if both the eigenvalues of $J(E^*)$ have negative (resp. positive) real part. On the other hand, the equilibrium point is called a saddle point when the eigenvalues have opposite sign.

Proposition 2.1. *The following statements hold for the system (2.2):*
(i) The trivial fixed point E_0 is always unstable.
(ii) The axial fixed point E_1 is always a saddle point. But the other axial fixed point E_2 is asymptotically stable for $a > \alpha$ and a saddle fixed point for $a < \alpha$.

Proof. (i) The eigenvalues of $J(E_0)$ are 1 and η and hence E_0 is always unstable.
(ii) The Jacobian matrix calculated at E_1 has one positive eigenvalue $\eta + \frac{b}{1+\alpha}$ and one negative eigenvalue -1. Hence, E_1 is a saddle point. The Jacobian calculated at E_2 is given by

$$J(E_2) = \begin{bmatrix} 1 - \frac{a}{\alpha} & 0 \\ \frac{b}{\alpha} & -\eta \end{bmatrix}. \tag{2.7}$$

Thus, E_2 is a saddle point for $\alpha > a$ with stable manifold along the v axis. On the other hand, E_2 becomes asymptotically stable for $\alpha < a$. □

It is difficult to determine the nature of co-existing equilibrium points such as E_1^*, E_2^* and E_3^* (whenever they exist) analytically due to the unavailability of explicit expression of these points. Existence of these equilibria and their stability in different regions depending on parameter values will be discussed in section 4.

3. Local Bifurcation Analysis

3.1. **Transcritical bifurcation**

Proposition 3.1. *The system (2.2) undergoes transcritical bifurcation at E_2 when α crosses the threshold $\alpha_{_{TC}} = a$.*

Proof. From (2.7), the Jacobian matrix $J(E_2)$ at $\alpha = \alpha_{_{TC}}$ has a zero eigenvalue. Let the eigenvectors corresponding to the zero eigenvalue of the Jacobian matrix and its transpose be $p = [\frac{\eta a}{b}, 1]^T$ and $q = [1, 0]^T$ respectively. Then transversality conditions [40] become

$$\begin{aligned} q^T \mathcal{F}_\alpha(E_2; \alpha = \alpha_{_{TC}}) &= 0, \\ q^T D\mathcal{F}_\alpha(E_2; \alpha = \alpha_{_{TC}})p &= \frac{\eta}{b} \neq 0, \\ q^T D^2\mathcal{F}(E_2; \alpha = \alpha_{_{TC}})(p, p) &= -2\,\frac{a\eta\,((a-1)\,\eta + b)}{b^2} \neq 0. \end{aligned}$$

Here, $\mathcal{F} = [F_1(u, v), F_2(u, v)]^T$ and all other notations are same as in [40]. Thus, the system (2.2) satisfies all the transversality conditions of transcritical bifurcation at E_2 for $\alpha = \alpha_{_{TC}}$. □

3.2. **Saddle-node bifurcation**

Whenever $a_2 < 0, a_1 > 0$ and $a_0 < 0$ hold, then the system (2.2) has either three co-existing equilibria or a unique co-existing equilibrium point. Suppose u_{s_1} and u_{s_2} are two real roots of $G'(u) = 0$ with $0 < u_{s_1} < u_{s_2}$. If $G(u_{s_1})$ and $G(u_{s_2})$ are of opposite sign, then three co-existing equilibria exist and we denote them by E_1^*, E_2^* and E_3^* with $u_1 < u_2 < u_3$. Now two cases may arise due to variation of one temporal parameter: either E_2^* coincides with E_1^* when $G(u_{s_1}) = 0$ or E_2^* coincides with E_3^* when $G(u_{s_2}) = 0$. Thus, two saddle-node bifurcations SN_I and SN_{II} occur for the first case and second case, respectively. We choose η as a saddle-node bifurcation parameter and the threshold value for SN_I is given by

$$\eta_{_{SN_I}} = \frac{abu_{s_1}}{\alpha(\alpha - a) - (\alpha^2 - 2\alpha + a)u_{s_1} + (1 - 2\alpha)u_{s_1}^2 - u_{s_1}^3}.$$

For the SN_{II} threshold value, u_{s_1} is replaced by u_{s_2} in the right side of the expression for $\eta_{_{SN_I}}$. The transversality conditions for this bifurcation is shown in the following prpstnosition.

Proposition 3.2. *The system (2.2) undergoes saddle-node bifurcation with respect to parameter η when $G(u) = 0$ has a double root.*

Proof. Suppose u_s is the double root of $G(u) = 0$, i.e., $G(u_s) = G'(u_s) = 0$ and $G''(u_s) \neq 0$ when $\eta = \eta_{SN}$. Let the corresponding equilibrium point be $E^*_{SN} = (u_s, v_s)$. Hence, the nontrivial nullclines $f_1(u, v) = 0$ and $f_2(u, v) = 0$ touch each other and they have same slope $\frac{dv^{(f_1)}}{du}|_{E^*_{SN}} = \frac{dv^{(f_2)}}{du}|_{E^*_{SN}}$ at E^*_{SN}. Now $\frac{dv^{(f)}}{du} = -\frac{\frac{\partial f}{\partial u}}{\frac{\partial f}{\partial v}}$ which implies

$$det(J(E^*_{SN})) = \left[uv \left(\frac{\partial f_1}{\partial u}\frac{\partial f_2}{\partial v} - \frac{\partial f_1}{\partial v}\frac{\partial f_2}{\partial u} \right) \right]_{E^*_{SN}} = 0.$$

Therefore, one of the eigenvalues of the Jacobian matrix $J(E^*_{SN})$ must be zero. Let $p = \left[1, \frac{\alpha b}{\eta(u_s+\alpha)^2}\right]^T$ and $q = \left[\frac{\eta\, v(u+\alpha)}{au}, -1\right]^T$ be the eigenvectors of $J(E^*_{SN})$ and $[J(E^*_{SN})]^T$ corresponding to zero eigenvalue respectively. Here, the transversality conditions become

$$q^T \mathcal{F}_\eta(E^*_{SN}; \eta = \eta_{SN}) = \frac{b u_s v_s}{\eta_{SN}(\alpha + u_s)} \neq 0, \tag{3.1a}$$

$$\begin{aligned} q^T D^2\mathcal{F}(E^*_{SN}; \eta = \eta_{SN})(p, p) = \frac{1}{a\alpha^2 u + 2\,a\alpha\, u^2 + a u^3}\Big[&- 8\,\alpha^2\eta\, uv - 10\,\alpha\,\eta\, u^2 v - 2\,\eta\, u^3 v - 2\,\alpha^3\eta + \\ &4\,\alpha^2\eta\, v + 2\,\alpha\,\eta\, u^2 + 4\,\alpha\,\eta\, uv - 2\,\alpha^2 b - 2\,\alpha^2\eta - 2\,\alpha\,\eta\, u \Big]\Big|_{E^*_{SN};\eta=\eta_{SN}} \neq 0. \end{aligned} \tag{3.1b}$$

Hence, the system (2.2) undergoes saddle-node bifurcation at $\eta = \eta_{SN}$. □

3.3. **Cusp bifurcation**

We have observed that two saddle-node bifurcation SN_I and SN_{II} occur at $E^*_{SN_I} = (u_{s_1}, v_{s_1})$ and $E^*_{SN_{II}} = (u_{s_2}, v_{s_2})$ for varying the bifurcation parameter η. If we alter another temporal parameter α, then $E^*_{SN_I}$ and $E^*_{SN_{II}}$ coincide at $E^*_{CP_1} = (u_{CP_1}, v_{CP_1})$ and these two saddle-node bifurcation curves SN_I and SN_{II} intersect at a cusp bifurcation point $(\eta_{CP_1}, \alpha_{CP_1})$ in the $\eta - \alpha$ parametric domain.

Proposition 3.3. *The system (2.2) passes through a cusp bifurcation when $G(u) = 0$ has a triple root.*

Proof. Suppose at $\eta = \eta_{CP_1}$ and $\alpha = \alpha_{CP_1}$, $G(u)$ has triple root u_{CP_1}, i.e., $G(u_{CP_1}) = G'(u_{CP_1}) = G''(u_{CP_1}) = 0$, where

$$u_{CP_1} = \frac{1}{3}(1 - 2\alpha).$$

Feasibility condition for $E^*_{CP_1} = (u_{CP_1}, v_{CP_1})$ comes from $a_2 < 0$. By following the same procedure as in Proposition 3.2, one can show that the Jacobian evaluated at $E^*_{CP_1}$ has a zero eigenvalue. Let an eigenvector of $J(E^*_{CP_1})$ and $[J(E^*_{CP_1})]^T$ corresponding to zero eigenvalue be p and q respectively. Then, the transversality condition (3.1b) for the cusp bifurcation becomes

$$q^T D^2\mathcal{F}(p, p)(E^*_{CP_1}; \eta = \eta_{CP_1}; \alpha = \alpha_{CP_1}) = 0,$$

which shows that the system (2.2) undergoes a codimension-2 cusp bifurcation at the threshold value $(\eta_{CP_1}, \alpha_{CP_1})$. Two saddle-node bifurcation curves SN_I and SN_{II} emerge from this cusp bifurcation point. The relationship between η_{CP_1} and α_{CP_1} is given by

$$\eta_{CP_1} = \frac{a\, b\, u_{CP_1}}{\alpha_{CP_1}(\alpha_{CP_1} - a) - (\alpha^2_{CP_1} - 2\alpha_{CP_1} + a)u_{CP_1} + (1 - 2\alpha_{CP_1})u^2_{CP_1} - u^3_{CP_1}}.$$

□

Proposition 3.4. *The system (2.2) undergoes another cusp bifurcation at E_2 when $G(0) = G'(0) = 0$.*

Proof. Suppose at $\eta = \eta_{CP_2}$ and $\alpha = \alpha_{CP_2}$, co-existing equilibria E_1^* and E_2^* coincide with the axial equilibrium point E_2. Then, $G(u)$ has a double root 0, i.e., $G(0) = 0 = G'(0)$ at the cusp bifurcation threshold. The expressions for η_{CP_2} and α_{CP_2} are given by

$$\alpha_{CP_2} = a, \quad \eta_{CP_2} = \frac{b}{1-a}.$$

Here, transcritical bifurcation curve intersects with saddle-node bifurcation curve SN_{II} at the cusp bifurcation point $(\eta_{CP_2}, \alpha_{CP_2})$ in the $\eta - \alpha$ plane. □

3.4. **Hopf Bifurcation**

A stable interior equilibrium E^* can lose its stability via Hopf Bifurcation when the trace of the Jacobian matrix evaluated at E^* changes from negative to positive value due to variation of a model parameter. Here, we choose α as a Hopf bifurcation parameter. The Jacobian matrix calculated at $E^*(u^*, v^*)$ is given by

$$J(E^*) = \begin{bmatrix} \frac{au^*v^*}{(u^*+\alpha)^2} - u^* & -\frac{au^*}{(u^*+\alpha)} \\ \frac{\alpha b v^*}{(u^*+\alpha)^2} & -\eta v^* \end{bmatrix}. \tag{3.2}$$

Now let us assume that $\alpha = \sqrt{\frac{au^*v^*}{u^*+\eta v^*}} - u^* \equiv \alpha_{_H}$, which is an implicit expression for α since (u^*, v^*) depends on α. Then, $T_{\alpha_{_H}} = tr[J(E^*; \alpha = \alpha_{_H})] = 0$. The system (2.2) undergoes a Hopf bifurcation at $\alpha = \alpha_{_H}$ if the following non-hyperbolicity and transversality conditions are satisfied:

$$C1: \quad D_{\alpha_{_H}} = det[J(E^*; \alpha = \alpha_{_H})] > 0,$$
$$C2: \quad \frac{d}{d\alpha}(tr[J(E^*)])|_{\alpha=\alpha_{_H}} \neq 0.$$

Proposition 3.5. *Interior equilibrium point E_1^* of the system (2.2) becomes unstable via Hopf bifurcation at $\alpha = \alpha_{_H}$.*

A Hopf-bifurcation is called supercritical (resp. subcritical) if the limit cycle generated at the Hopf-bifurcation is stable (resp. unstable). Explicit expression of Hopf bifurcation threshold is hard to find due to the lack of explicit expression of the co-existing fixed point. But we can verify these results numerically. If we fix the temporal parameters $a = 0.2, b = 0.15$ and $\eta = 0.095$, then the system (2.2) undergoes subcritical Hopf bifurcation around $E_1^* = (0.04801, 1.28156)$ for $\alpha_{_H} = 0.22122$. For the same set of parameter values except $\eta = 0.095$, supercritical Hopf bifurcation observed around $E_1^* = (0.04763, 1.29246)$ for $\alpha_H = 0.22379$.

3.5. **Bautin Bifurcation**

We have seen that the co-existing equilibrium point E_1^* changes its stability either through a supercritical or a subcritical Hopf bifurcation. A supercritical Hopf corresponds to the first Lyapunov coefficient $l_1 > 0$ in which a stable limit cycle is formed. On the other hand, first Lyapunov coefficient l_1 is negative in subcritical Hopf bifurcation and an unstable limit cycle arises. In case of zero first Lyapunov coefficient, the system (2.2) passes through a codimension-2 bifurcation called a generalized Hopf bifurcation (GH) or a Bautin bifurcation.

Proposition 3.6. *If the first Lyapunov coefficient l_1 becomes zero for $\alpha = \alpha_{_{GH}}$ and $\eta = \eta_{_{GH}}$, then system (2.2) undergoes a Bautin or GH bifurcation.*

Analytical expression and transversality conditions for this bifurcation are hard to find due to the same reason mentioned before. But numerically we verify that for parameter values $a = 0.2$ and $b = 0.15$, the system (2.2) undergoes two Bautin bifurcation at $\alpha_{_{GH_1}} = 0.23412$ and $\eta_{_{GH_1}} = 0.09399$ and at $\alpha_{_{GH_2}} = 0.22049$ and $\eta_{_{GH_2}} = 0.09705$.

3.6. **Bogdanov-Takens Bifurcation**

We have observed that system (2.2) has two saddle-node bifurcation curves and two Hopf bifurcation curves in the $\eta - \alpha$ parametric plane. When one Hopf bifurcation curve intersects with a saddle-node bifurcation curve then a codimension-2 bifurcation occurs. This bifurcation is called Bogdanov-Takens (BT) bifurcation. Generally, BT bifurcation occurs at a fixed point when both the trace and the determinant of the Jacobian matrix evaluated at that point vanish.

Proposition 3.7. *The system (2.2) undergoes a Bogdanov-Takens Bifurcation at E_1^* or E_3^* if the Jacobian matrix at E_1^* or E_3^* has zero eigenvalue of multiplicity two.*

Again, it is difficult to find analytical expressions and corresponding transversality conditions for the BT bifurcation since explicit expressions for co-existing equilibria are not available. However, we choose η and α as bifurcation parameters and verify the existence of BT bifurcation numerically for the system (2.2). For this, we fix other parameters at $a = 0.2$, $b = 0.15$ and find that the system (2.2) undergoes a BT bifurcation for E_1^* at $(\eta_{_{BT_1}}, \alpha_{_{BT_1}}) = (0.10037, 0.22556)$ and another BT bifurcation for E_3^* at $(\eta_{_{BT_2}}, \alpha_{_{BT_2}}) = (0.12413, 0.21001)$.

4. Bifurcation diagram

Here we discuss the global and local bifurcation results of the system (2.2) obtained with the help of Matlab software package. We present a bifurcation diagram in the two-dimensional $\eta - \alpha$ plane for fixed values of $a = 0.2$ and $b = 0.15$. The bifurcation threshold values are very close to each other. For example, if we take $\eta = 0.1$, then the values of other bifurcation thresholds are $\alpha_{_{SN_I}} = 0.22604$, $\alpha_{_{SN_{II}}} = 0.226098$, $\alpha_{_{H_1}} = 0.226044$ and $\alpha_{_{SNLC_I}} = 0.226184$. These values won't be clearly visible in actual bifurcation plot. Hence, a schematic bifurcation diagram is plotted in Fig. 2 for better visualisation. Here, $\alpha_{_{SNLC_I}}$ denotes the threshold value of saddle node bifurcation of limit cycle at which an unstable limit cycle and a stable limit cycle surrounding an interior equilibrium point coincide.

There are local as well as global bifurcation curves. Local bifurcation curves include saddle-node bifurcation curve (blue color curve), transcritical bifurcation curve (cyan color curve) and Hopf bifurcation curve (red color curve). On the other hand global bifurcation curves include saddle-node bifurcation of limit cycle (green color curve) and homoclinic curve (magenta and brown color curves). These curves divide the $\eta - \alpha$ plane into fourteen regions $R_1 - R_{14}$. From Proposition 3.2, the trivial equilibrium E_0 is unstable and axial equilibrium point E_1 is a saddle for all the regions. However, the other axial equilibrium point E_2 is stable in regions R_5 and R_6, and a saddle point elsewhere. Now we discuss the behavior of the interior equilibrium points of the system (2.2) in each region and the changes in dynamical behavior across the bifurcation curves. Dynamics of each region is listed in Table 1 and schematic phase portraits (for clarity) of the co-existing equilibria in each region are plotted in Fig. 3. It is seen that the regions R_1, R_7 have similar dynamics and so are the regions R_{11}, R_{13}.

We first discuss local bifurcation curves across which number of equilibria or stability change with the variation of parameters. Fig. 2 shows that two saddle-node bifurcation curves emerge from a cusp bifurcation point $CP_1(\eta_{_{CP_1}}, \alpha_{_{CP_1}}) \equiv (0.099, 0.227)$ which is a codimension-2 bifurcation point. We denote the lower and upper saddle-node bifurcation curves by SN_I and SN_{II} respectively. The system (2.2) has three interior equilibria E_1^*, E_2^* and E_3^* in the region bounded by SN_I, SN_{II} and the transcritical bifurcation curve (TC) parallel to η-axis. We label the three equilibria E_1^*, E_2^* and E_3^* such that their u-components satisfy $0 < u_1 < u_2 < u_3$. Among them E_2^* is always saddle and the nature of E_1^* and E_3^* depend on the Hopf bifurcation curve. In region R_2, E_1^* is an unstable node, E_2^* is saddle and E_3^* is a stable node. E_1^* and E_2^* collide and disappear across the SN_{II} curve leading to a unique equilibrium point. Whenever the system (2.2) has only a unique co-existing equilibrium point then we label it as E_1^*. Thus, the system has unique co-existing equilibrium point E_1^* in R_1, which is globally asymptotically stable. Hopf curves meet with saddle-node bifurcation curves at codimension-2 BT bifurcation points BT_1 and BT_2. We denote Hopf curves emanating from BT_1 and BT_2 by H_1 and H_2 respectively. Stability of co-existing equilibrium point changes when α crosses the Hopf threshold value $\alpha_{_{H_1}}$ or

$\alpha_{_{H_2}}$. There are another two codimension-2 Bautin (or GH) bifurcation points GH_1 and GH_2 on the Hopf curves H_1 and H_2 respectively, where the first Lyapunov co-efficient (l_1) vanishes. A sub-critical (resp. super-critical) Hopf bifurcation occurs across each Hopf curve to the right (resp. left) of the GH point. Numerical threshold values of the GH and BT bifurcation points have already been given. TC curve intersects with SN_{II} curve at another cusp bifurcation point CP_2 (0.2,0.1875). Interior equilibrium E_1^* and axial equilibrium E_2 exchange their stability across TC. However, E_1^* becomes infeasible in region R_5 and hence the system (2.2) has two co-existing equilibria E_2^* (saddle) and E_3^* (stable node) in R_5. The stable manifolds of E_2^* separates the basins of attraction E_2 and E_3^*. E_2^* and E_3^* collide through saddle-node bifurcation (across SN_I) and disappear in region R_6. Thus, the system (2.2) has no co-existing equilibrium point and E_2 is globally asymptotically stable in R_6. From R_6 to R_7 across TC curve, axial point E_2 becomes unstable and E_1^* again becomes feasible. Hence, E_1^* is globally asymptotically stable in region R_7.

Now we discuss global bifurcations which occur when there is a collision between two periodic orbits or a periodic orbit and an equilibrium point. A saddle-node bifurcation curve of limit cycles ($SNLC_I$) emerges from the GH_1 point and meets with the SN_{II} curve. On the $SNLC_I$ curve, an unstable limit cycle surrounding E_1^* generated from subcritical Hopf bifurcation coincides with a stable limit cycle. Therefore, stable equilibrium point E_1^* is surrounded by an unstable limit cycle inside a stable limit cycle in R_{13}. A homoclinic curve (HC_I) emerges from the BT_1 point and ends at the intersection point of $SNLC_I$ and SN_{II} curves. HC_1 corresponds to the appearance or disappearance of an unstable limit cycle around the co-existing fixed point E_1^*. A second

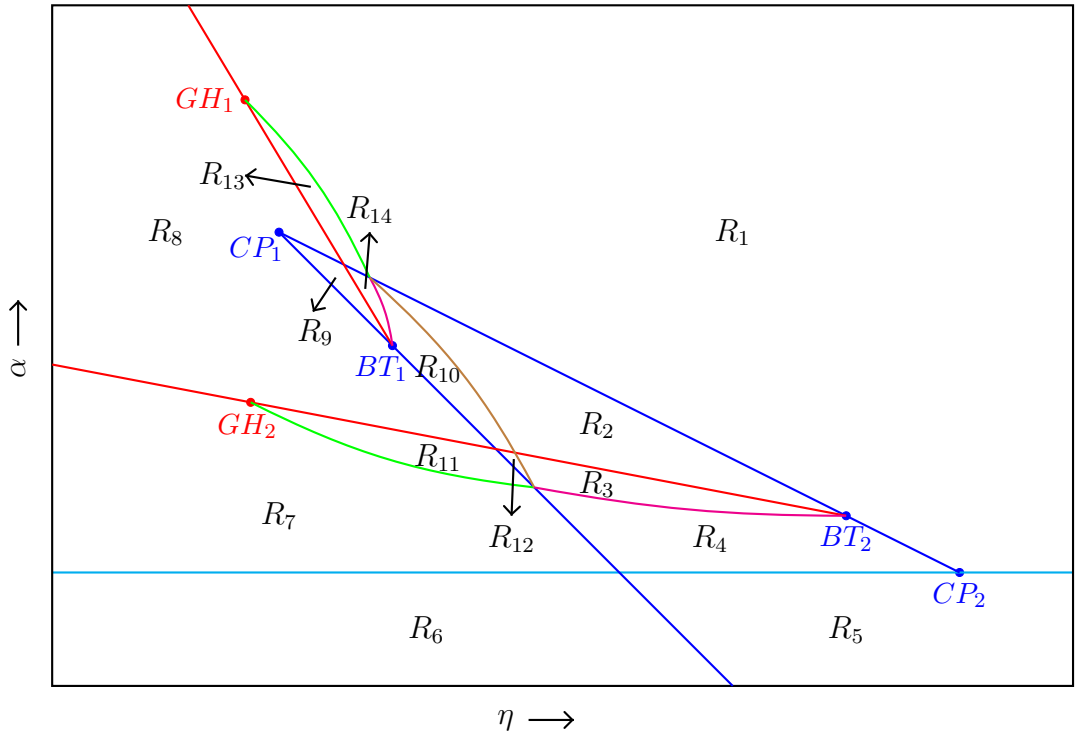

FIGURE 2. Schematic bifurcation diagram in $\eta - \alpha$ plane. Cyan, blue and red color curves respectively represent transcritical, saddle-node and Hopf bifurcation curves. Green color curve from GH point represents saddle-node bifurcation of limit cycle and magenta color curve from BT point represents homoclinic orbit. Another global homoclinic bifurcation curve is represented by brown color curve.

Region (phase dynamics)	Interior equilibria			Remarks
	E_1^*	E_2^*	E_3^*	
R_1 (Fig. 3a)	Stable	-	-	-
R_2 (Fig. 3b)	Unstable	Saddle	Stable	-
R_3 (Fig. 3c)	Stable	Saddle	Stable	E_1^* is encircled by an unstable limit cycle.
R_4 (Fig. 3d)	Stable	Saddle	Stable	There is a bistablity between E_1^* and E_3^*.
R_5 (Fig. 3e)	-	Saddle	Stable	There is a bistablity between axial fixed point E_2 and interior fixed point E_3^*.
R_6 (Fig. 3f)	-	-	-	Axial equilibrium E_2 is asymptotically stable.
R_7 (Fig. 3a)	Stable	-	-	-
R_8 (Fig. 3g)	Unstable	-	-	A stable Hopf bifurcating limit cycle appears around the co-existing fixed point E_1^*.
R_9 (Fig. 3h)	Unstable	Saddle	Unstable	All the interior equilibrium points lie inside a stable limit cycle.
R_{10} (Fig. 3i)	Unstable	Saddle	Stable	E_1^*, E_2^*, E_3^* are surrounded by a stable limit cycle and the system shows bistable phenomena where the stable limit cycle and a stable co-existing equilibrium point act as attractor.
R_{11} (Fig. 3j)	Stable	-	-	E_1^* is encircled by an unstable limit cycle which is again encircled by a stable limit cycle.
R_{12}(Fig. 3k)	Stable	Saddle	Stable	An unstable limit cycle containing E_1^*, E_2^* and E_3^* are surrounded by a stable limit cycle.
R_{13} (Fig. 3j)	Stable	-	-	Same characteristic as in R_{11}.
R_{14} (Fig. 3l)	Unstable	Saddle	Stable	A stable limit cycle surrounds all the co-existing fixed points.

TABLE 1. Dynamical behaviour of the interior equilibria in each region for the system (2.2). Axial fixed point E_2 is saddle in all regions except in R_5 and R_6 where it is stable.

saddle-node bifurcation curve of limit cycles ($SNLC_{II}$) from the GH_2 point and a homoclinic curve (HC_{II}) from the BT_2 point meet at a point on the SN_I curve.

Another homoclinic curve HC_{III} (brown color curve) extends from the intersection point of HC_I, $SNLC_I$ and SN_{II} to the intersection point of HC_{II}, $SNLC_{II}$ and SN_I. Along the HC_{III} curve, a large stable limit cycle containing all the co-existing equilibria E_1^*, E_2^* and E_3^* appears or disappears. There is bistablity between the stable limit cycle and the co-existing fixed point E_3^* in R_{10} and the stable manifold of the saddle point E_2^* separates their basin of attraction.

5. Spatio-temporal model

Now we take the spatial effects into account by including the diffusion terms. For simplicity, we consider the spatio-temporal model in one dimension. Let $\Omega = (0, L)$ be a bounded domain with boundary $\partial\Omega = \{0, L\}$. The governing equations are

$$\begin{cases} \frac{\partial u}{\partial t} = \frac{\partial^2 u}{\partial x^2} + u(1-u) - \frac{auv}{\alpha+u}, & x \in \Omega,\ t > 0, \\ \frac{\partial v}{\partial t} = d\frac{\partial^2 v}{\partial x^2} + \eta v(1-v) + \frac{buv}{\alpha+u}, & x \in \Omega,\ t > 0, \\ \frac{\partial u}{\partial x} = \frac{\partial v}{\partial x} = 0, & x \in \partial\Omega,\ t > 0, \\ u(0,x) = u_0(x) \geq 0, \quad v(0,x) = v_0(x) \geq 0, & x \in \Omega, \end{cases} \tag{5.1}$$

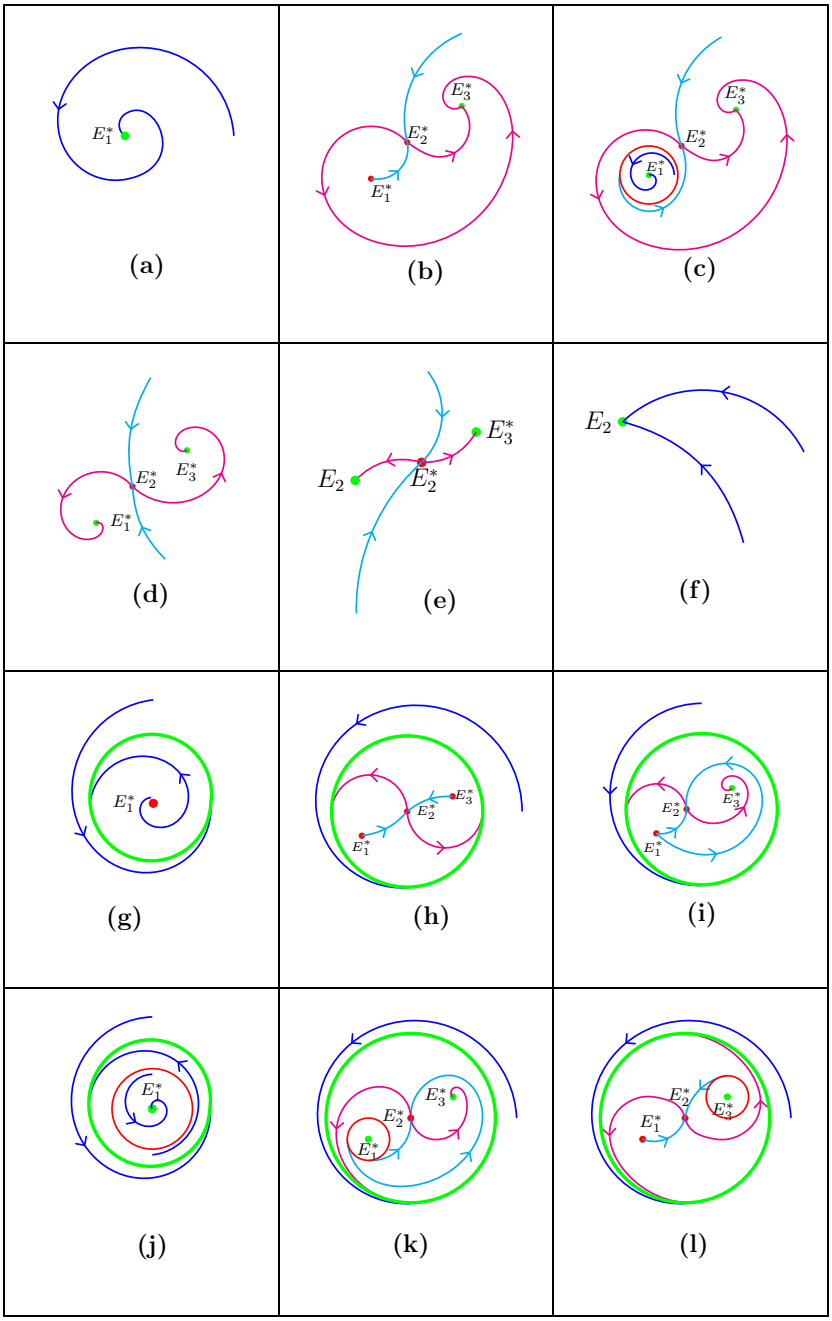

FIGURE 3. Schematic phase portrait diagram. Here green circle represents stable limit cycle and red circle represents unstable limit cycle. Stable and unstable manifolds of saddle point are denoted by cyan and magenta color curves respectively.

where d represents the ratio of diffusion coefficients of predator and prey. Next we discuss existence of global solution in subsection 5.1, existence of positive steady state solution in subsection 5.2 and stability of homogeneous steady states in subsection 5.3. The results obtained are applicable in higher dimensions as well. Hence, we take ∇^2 for Laplacian and $\frac{\partial}{\partial n}$ for normal derivative in subsections 5.1 to 5.3.

5.1. **Existence of global solution**

The local existence of unique solution of the system (5.1) is easy to establish by standard existence theory [41,42]. Here, we prove the global existence by showing the boundedness of $||u(t,.)||_{L_\infty}$, $||v(t,.)||_{L_\infty}$ for all finite time t. Let $D_T = (0,T] \times \Omega$ and $S_T = (0,T] \times \partial\Omega$. To prove the global existence, we make use of the following strong comparison theorem [33,43]:

Theorem 5.1. *Let $\vec{p}(t,x) = (p_1(t,x), \cdots, p_m(t,x))^T$ and $\vec{q}(t,x) = (q_1(t,x), \cdots, q_m(t,x))^T$, $m \geq 1$, be two vector functions that satisfy the following conditions (where inequalities satisfy component-wise):*

(a) *For each i, we have both $p_i, q_i \in C(\bar{D}_T) \cap C^{1,2}(D_T)$ with $\vec{p}(0,x) \leq \vec{q}(0,x)$ for $x \in \Omega$,*

(b) *$\vec{p}_t - \mathcal{D}\nabla^2\vec{p} - \vec{f}(t,x;\vec{p}) \leq \vec{q}_t - \mathcal{D}\nabla^2\vec{q} - \vec{f}(t,x;\vec{q})$ in D_T, where $\mathcal{D} = diag(D_1, \cdots, D_m)$ and $\vec{f}(t,x,\vec{p}) = (f_1(t,x,\vec{p}), \cdots, f_m(t,x,\vec{p}))^T$. Here, each f_i is Hölder continuous for $(t,x) \in \bar{D}_T$ and continuously differentiable with respect to each of the components $p_1, p_2, \cdots, p_m$. Further, each f_i is quasi-monotonically increasing in $\vec{p}$, i.e.,*

$$\frac{\partial f_i(t,x,\vec{p})}{\partial p_j} \geq 0,\ \vec{p} = (p_1, \cdots, p_m),\ i,j = 1, \cdots, m,\ \ i \neq j,$$

(c) *$\frac{\partial \vec{p}}{\partial n} = \frac{\partial \vec{q}}{\partial n} = 0$ in S_T.*

Then, $\vec{p}(t,x) \leq \vec{q}(t,x)$ in $\bar{D}_T$.

Proposition 5.2. *For any non-negative initial condition $u_0(x),\ v_0(x) \in C^2(\Omega)$ with*

$$u_0(x) \leq 1 \text{ and } v_0(x) \leq \frac{(\eta + b)}{\eta},$$

the system (5.1) has unique global and bounded solution for all $t \geq 0$.

Proof. Using Lemma 14.20 of [33], it can be shown that $u(t,x) \geq 0$ and $v(t,x) \geq 0$ for any non-negative initial condition $u_0(x),\ v_0(x)$. Let $A(t) = \frac{A_0}{A_0 + (1-A_0)e^{-t}}$ be the solution of the initial value problem

$$\begin{cases} \frac{dA}{dt} = A(1-A) \quad \text{for } t > 0, \\ A(0) = A_0 = \max_\Omega u_0(x) \leq 1. \end{cases}$$

Consider the following problem:

$$\begin{cases} \frac{\partial u}{\partial t} - \nabla^2 u - u(1-u) \leq 0 = \frac{\partial A}{\partial t} - \nabla^2 A - A(1-A) \quad \text{in } D_T, \\ \frac{\partial u}{\partial n} = \frac{\partial A}{\partial n} = 0 \quad \text{in } S_T, \\ u(0,x) = u_0(x) \leq A_0 \quad \text{in } \Omega. \end{cases}$$

Then, using Theorem 5.1, we conclude that $u(t,x) \leq A_0 \leq 1$ and hence $u(t,x) \leq 1$ in $\bar{D}_T$.

To show the boundedness of v, we consider the initial value problem

$$\begin{cases} \frac{dB}{dt} = (\eta + b)B - \eta B^2 \quad \text{for } t > 0, \\ B(0) = B_0 = \max_\Omega v_0(x) \leq \frac{(\eta+b)}{\eta}. \end{cases} \tag{5.2}$$

The solution of the system (5.2) is

$$B(t) = \frac{(\eta + b)B_0}{\eta B_0 + \{(1 - B_0)\eta + b\}e^{-(\eta+b)t}}.$$

From second equation of system (5.1), we obtain

$$\frac{\partial v}{\partial t} - d\nabla^2 v - \eta v(1-v) - bv \leq 0 = \frac{\partial v}{\partial t} - d\nabla^2 v - \eta v(1-v) - \frac{buv}{u+\alpha}.$$

Now we form the problem

$$\begin{cases} \frac{\partial v(t,x)}{\partial t} - d\nabla^2 v - \eta v(1-v) - bv \leq \frac{\partial B}{\partial t} - d\nabla^2 B - \eta B(1-B) - bB & \text{in } D_T, \\ \frac{\partial v}{\partial n} = \frac{\partial B}{\partial n} = 0 & \text{in } S_T, \\ v(0,x) = v_0(x) \leq B_0 & \text{in } \Omega. \end{cases}$$

Then, using Theorem 5.1, we find $v(t,x) \leq B_0$ and hence $v(t,x) \leq \frac{(\eta+b)}{\eta}$ in $\bar{D}_T$. Thus, $||u(t,.)||_{L_\infty}$, $||v(t,.)||_{L_\infty}$ are bounded for all finite t. □

5.2. **Existence of positive steady state solutions**

A steady state solution $(u(x), v(x))$ of the system (5.1) satisfy

$$\begin{cases} \nabla^2 u(x) + F_1(u(x), v(x)) = 0 & x \in \Omega, \\ d\nabla^2 v(x) + F_2(u(x), v(x)) = 0 & x \in \Omega, \\ \frac{\partial u}{\partial n} = \frac{\partial v}{\partial n} = 0 & x \in \partial\Omega. \end{cases} \tag{5.3}$$

Proposition 5.3. *If the system (5.3) satisfies the conditions $a < 1$ and $\alpha - a + 1 - M > 0$, where M satisfies*

$$M \geq 1 + \frac{b}{\eta(1+\alpha)},$$

then the system (5.3) has at least one positive steady state solution $(u(x), v(x))$.

Proof. For $u \geq 0$ and $v \geq 0$,

$$\frac{\partial F_1}{\partial v} = -\frac{au}{u+\alpha} \leq 0, \qquad \frac{\partial F_2}{\partial u} = \frac{bv\alpha}{(u+\alpha)^2} \geq 0.$$

Hence, the system (5.3) is a mixed quasi-monotone [33, 44]. Now, an upper solution $(\overline{u}(x), \overline{v}(x))$ and lower solution $(\underline{u}(x), \underline{v}(x))$ of the system (5.3) satisfy the following:

$$-\nabla^2 \overline{u} - F_1(\overline{u}, \underline{v}) \geq 0 \geq -\nabla^2 \underline{u} - F_1(\underline{u}, \overline{v}), \quad x \in \Omega, \tag{5.4}$$

$$-d\nabla^2 \overline{v} - F_2(\overline{u}, \overline{v}) \geq 0 \geq -d\nabla^2 \underline{v} - F_2(\underline{u}, \underline{v}), \quad x \in \Omega, \tag{5.5}$$

$$\frac{\partial \overline{u}}{\partial n} \geq 0 \geq \frac{\partial \underline{u}}{\partial n}, \quad \frac{\partial \overline{v}}{\partial n} \geq 0 \geq \frac{\partial \underline{v}}{\partial n}, \quad x \in \partial\Omega.$$

To prove the existence of positive steady state, we construct a pair of upper and lower solutions $(\overline{u}(x), \overline{v}(x))$ and $(\underline{u}(x), \underline{v}(x))$ of the system (5.3).

Observe that $\overline{u}(x) = 1$ satisfies the left hand side of the inequality (5.4) for any $\underline{v}(x) \geq 0$. The left hand side of the inequality (5.5) is satisfied for $\overline{v}(x) = M$, where M is a positive constant such that

$$M \geq 1 + \frac{b}{\eta(1+\alpha)}.$$

We also require $\overline{v}(x) = M$ to satisfy the right hand side of the inequality (5.4), i.e.,

$$-\nabla^2 \underline{u} - \underline{u}(1 - \underline{u} - \frac{aM}{\underline{u}+\alpha}) \leq 0 \quad \text{for } x \in \Omega. \tag{5.6}$$

For $a < 1$ and $\alpha - a + 1 - M > 0$, it is easy to verify that $\underline{u}(x) = 1 - a$ satisfies the inequality (5.6). For the given $\underline{u}(x) = 1 - a$ with $a < 1$ and $1 - a + \alpha > M$, if we choose $\underline{v}(x)$ to be a small positive constant such that

$$0 < \underline{v}(x) < 1 + \frac{b(1-a)}{\eta(1-a+\alpha)} \quad \text{for } x \in \Omega,$$

then the right hand side of the inequality (5.5) is satisfied. Thus, we have constructed a pair of positive upper and lower solutions $(\overline{u}(x), \overline{v}(x))$ and $(\underline{u}(x), \underline{v}(x))$ of the system (5.3). This completes the proof. □

5.3. **Homogeneous steady state solution analysis**

The system (5.1) has zero steady state $E_0(0,0)$, two axial steady states $E_1(1,0)$ and $E_2(0,1)$ and co-existing steady state $E^*(u^*, v^*)$ which satisfies $f_1(u^*, v^*) = 0$ and $f_2(u^*, v^*) = 0$. Consider the linearized system around a steady state $E = (u, v)$

$$\frac{\partial W}{\partial t} = \mathcal{D}\nabla^2 W + J(u,v)W, \tag{5.7}$$

where $\mathcal{D}$ =diag$(1, d)$, $W = (w_1, w_2)^T$ and $J(u, v)$ is the Jacobian matrix calculated at the steady state $E(u, v)$.

Proposition 5.4. *Steady state solution $E_0(0,0)$ is always unstable.*

Proof. Linearized system (5.7) around E_0 becomes

$$\begin{cases} \frac{\partial w_1}{\partial t} = \nabla^2 w_1 + w_1 & \text{in } D_T, \\ \frac{\partial w_2}{\partial t} = d\nabla^2 w_2 + \eta w_2 & \text{in } D_T, \\ \frac{\partial w_1}{\partial n} = \frac{\partial w_2}{\partial n} = 0 & \text{in } S_T. \end{cases}$$

Now E_0 is unstable if the largest eigenvalue of the corresponding eigenvalue problem

$$\begin{cases} \nabla^2 w_1 + w_1 = \lambda w_1, & x \in \Omega, \\ d\nabla^2 w_2 + \eta w_2 = \lambda w_2, & x \in \Omega, \\ \frac{\partial w_1}{\partial n} = \frac{\partial w_2}{\partial n} = 0, & x \in \partial\Omega, \end{cases} \tag{5.8}$$

is positive. Let λ_m be the largest eigenvalue of the system (5.8). Note that the principal eigenvalue λ_1 of the system

$$\begin{cases} \nabla^2 w_1 + w_1 = \lambda w_1, & x \in \Omega, \\ \frac{\partial w_1}{\partial n} = 0, & x \in \partial\Omega, \end{cases}$$

is positive with corresponding eigenfunction $\tilde{w}_1$. But, λ_1 is also an eigenvalue of the system (5.8) with the eigenfunction $(\tilde{w_1}, 0)^T$. Therefore, $\lambda_m \geq \lambda_1 > 0$. This completes the proof. □

Proposition 5.5. *Steady state solution $E_1(1,0)$ is unstable.*

Proof. Linearizing system (5.7) about E_1 we get

$$\begin{cases} \frac{\partial w_1}{\partial t} = \nabla^2 w_1 - w_1 - \frac{a}{1+\alpha} w_2 & \text{in } D_T, \\ \frac{\partial w_2}{\partial t} = d\nabla^2 w_2 + (\eta + \frac{b}{1+\alpha}) w_2 & \text{in } D_T, \\ \frac{\partial w_1}{\partial n} = \frac{\partial w_2}{\partial n} = 0 & \text{in } S_T. \end{cases}$$

E_1 is unstable if the largest eigenvalue $\lambda = \lambda_m$ of the corresponding eigenvalue problem

$$\begin{cases} \nabla^2 w_1 - w_1 - \frac{a}{1+\alpha} w_2 = \lambda w_1, & x \in \Omega, \\ d\nabla^2 w_2 + (\eta + \frac{b}{1+\alpha}) w_2 = \lambda w_2, & x \in \Omega, \\ \frac{\partial w_1}{\partial n} = \frac{\partial w_2}{\partial n} = 0, & x \in \partial\Omega, \end{cases} \tag{5.9}$$

is positive. Now the principal eigenvalue λ_1 of

$$\begin{cases} d\nabla^2 w_2 + (\eta + \frac{b}{1+\alpha})w_2 = \lambda w_2, & x \in \Omega, \\ \frac{\partial w_2}{\partial n} = 0, & x \in \partial\Omega, \end{cases}$$

is positive with corresponding eigenfunction $\tilde{w}_2$. Let $\tilde{w}_1$ be the solution of the linear problem

$$\begin{cases} \nabla^2 w_1 - (1 + \lambda_1)w_1 = \frac{a}{1+\alpha}\tilde{w}_2, & x \in \Omega, \\ \frac{\partial w_1}{\partial n} = 0, & x \in \partial\Omega. \end{cases}$$

Then, λ_1 is also an eigenvalue of the system (5.9) with the eigenfunction $(\tilde{w_1}, \tilde{w_2})^T$. Therefore, $\lambda_m \geq \lambda_1 > 0$. Hence the proof is complete. □

Proposition 5.6. *Steady state solution $E_2(0, 1)$ is unstable for $\alpha > a$ and stable for $\alpha < a$.*

Proof. Linearized system (5.7) about E_2 is

$$\begin{cases} \frac{\partial w_1}{\partial t} = \nabla^2 w_1 + (1 - \frac{a}{\alpha})w_1 & \text{in } D_T, \\ \frac{\partial w_2}{\partial t} = d\nabla^2 w_2 + \frac{b}{\alpha}w_1 - \eta w_2 & \text{in } D_T, \\ \frac{\partial w_1}{\partial n} = \frac{\partial w_2}{\partial n} = 0 & \text{in } S_T. \end{cases}$$

Corresponding eigenvalue problem is

$$\begin{cases} \nabla^2 w_1 + (1 - \frac{a}{\alpha})w_1 = \lambda w_1, & x \in \Omega, \\ d\nabla^2 w_2 + \frac{b}{\alpha}w_1 - \eta w_2 = \lambda w_2, & x \in \Omega, \\ \frac{\partial w_1}{\partial n} = \frac{\partial w_2}{\partial n} = 0, & x \in \partial\Omega. \end{cases} \tag{5.10}$$

If the largest eigenvalue λ_m of the system (5.10) is positive then E_2 is unstable and stable otherwise. The principal eigenvalue λ_1 of the system

$$\begin{cases} \nabla^2 w_1 + (1 - \frac{a}{\alpha})w_1 = \lambda w_1, & x \in \Omega, \\ \frac{\partial w_1}{\partial n} = 0, & x \in \partial\Omega, \end{cases} \tag{5.11}$$

is positive for $\alpha > a$ with corresponding eigenfunction $\tilde{w}_1$. Suppose that $\tilde{w}_2$ is the solution of the linear problem

$$\begin{cases} d\nabla^2 w_2 - (\eta + \lambda_1)w_2 = -\frac{b}{\alpha}\tilde{w}_1, & x \in \Omega, \\ \frac{\partial w_2}{\partial n} = 0, & x \in \partial\Omega. \end{cases}$$

Then, λ_1 is also an eigenvalue of the system (5.10) with the eigenfunction $(\tilde{w_1}, \tilde{w_2})^T$. Therefore, $\lambda_m \geq \lambda_1 > 0$. Hence, E_2 is unstable for $\alpha > a$.

For $\alpha < a$, let $(\tilde{w_1}, \tilde{w_2})^T$ be the eigenfunction of the system (5.10) corresponding to the largest eigenvalue λ_m. If $\tilde{w}_1 \neq 0$, then λ_m is also an eigenvalue of the system (5.11) corresponding to eigenfunction $\tilde{w}_1$. Now $\alpha < a$ implies $\lambda_m < 0$. If $\tilde{w}_1 = 0$, then $\tilde{w}_2 \neq 0$ and λ_m becomes an eigenvalue with eigenfunction $\tilde{w}_2$ for the problem

$$\begin{cases} d\nabla^2 w_2 - \eta w_2 = \lambda w_2, & x \in \Omega, \\ \frac{\partial w_2}{\partial n} = 0, & x \in \partial\Omega. \end{cases} \tag{5.12}$$

Clearly, the largest eigenvalue of the system (5.12) is $-\eta < 0$ and hence $\lambda_m < 0$. As a result, the steady state solution $E_2(0, 1)$ is stable for $\alpha < a$. □

Proposition 5.7. *Steady state solution* $E^*(u^*, v^*)$ *is stable if* $\frac{(u^*+\alpha)^2}{v^*} > a$.

Proof. The linearized system about E^* is

$$\frac{\partial W}{\partial t} = \mathcal{D}\nabla^2 W + JW, \tag{5.13}$$

where $\mathcal{D} = \text{diag}(1, d)$, W is a two-dimensional column vector and

$$J = \begin{bmatrix} \frac{au^*v^*}{(u^*+\alpha)^2} - u^* & -\frac{au^*}{(u^*+\alpha)} \equiv \\ \frac{\alpha b v^*}{(u^*+\alpha)^2} & -\eta v^* \end{bmatrix} \equiv \begin{bmatrix} a_{10} & a_{01} \\ b_{10} & b_{01} \end{bmatrix}.$$

Let $0 = k_1 < k_2 < \cdots < k_j < \cdots$ be the eigenvalues and $E(k_j)$ be the eigenfunction space corresponding to k_j for the eigenvalue problem

$$\begin{aligned} -\nabla^2 w &= kw, && \text{in } \Omega, \\ \frac{\partial w}{\partial n} &= 0, && \text{on } \partial\Omega. \end{aligned}$$

Further, suppose that $\{\psi_{i,j} : i = 1, \cdots, \dim\big(E(k_j)\big)\}$ be the orthogonal basis set of $E(k_j)$ and $X_{ij} = \{c\psi_{i,j} : c = (c_1, c_2)^T\}$. Let $X_j = \bigoplus_{i=1}^{\dim(E(k_j))} X_{ij}$ be the direct sum of X_{ij} and $\Psi = \bigoplus_{i=1}^{\infty} X_i$. We expand the solution W as

$$W(t, x) = \sum_{j=0}^{\infty} C_j \psi_j, \tag{5.14}$$

where $C_j(t)$ is a two-dimensional column vector and $\psi_j(x) \in \Psi$. Substituting (5.14) into (5.13) and equating the coefficient of each ψ_j, we find

$$\frac{\partial C_j}{dt} = L_j C_j \quad \text{where } L_j = J - k_j \mathcal{D}.$$

Now, E^* is stable if and only if both the eigenvalues of the matrix L_j, for each $j \geq 1$, have negative real parts. This is guaranteed when the trace of L_j and determinant of L_j become negative and positive respectively. The trace of L_j is $a_{10} + b_{01} - (1 + d)k_j$, which becomes negative if $a_{10} < 0$ since $b_{01} < 0$. The determinant of L_j

$$dk_j^2 - (da_{10} + b_{01})k_j^2 + (a_{10}b_{01} - a_{01}b_{10})$$

is also positive for $a_{10} < 0$ since $a_{01} < 0$ and $b_{10} > 0$. Now $a_{10} < 0$ implies $\frac{(u^*+\alpha)^2}{v^*} > a$. Thus, steady state solution E^* is stable if $\frac{(u^*+\alpha)^2}{v^*} > a$. □

5.4. **Turing instability**

We consider the parameter restriction $\eta < \eta_{_{CP_1}}$ and $\alpha > a$ so that the local model (5.1) has unique co-existing homogeneous steady state $E^*(u^*, v^*)$. For Turing instabilities, the homogeneous steady state solution is stable under the absence of diffusion, i.e., $a_{10} + b_{01} < 0$ and $(a_{10}b_{01} - a_{01}b_{10}) > 0$. To check Turing instability, we introduce spatial perturbation around E_* by $u = u_* + \epsilon\bar{u}e^{(\lambda t + ikx)}$ and $v = v_* + \epsilon\bar{v}e^{(\lambda t + ikx)}$, where $|\epsilon| << 1$. Substituting u and v into the system (5.1) and linearizing we find

$$S_k \begin{bmatrix} \bar{u} \\ \bar{v} \end{bmatrix} \equiv \begin{bmatrix} a_{10} - k^2 - \lambda & a_{01} \\ b_{10} & b_{01} - dk^2 - \lambda \end{bmatrix} \begin{bmatrix} \bar{u} \\ \bar{v} \end{bmatrix} = \begin{bmatrix} 0 \\ 0 \end{bmatrix}. \tag{5.15}$$

For non-trivial solution of the system (5.15) we have $\det(S_k) = 0$, which leads to

$$\lambda^2 - T(k^2)\lambda + H(k^2) = 0, \tag{5.16}$$

where

$$T(k^2) = a_{10} + b_{01} - (1+d)k^2 \quad \text{and} \quad H(k^2) = dk^4 - (da_{10} + b_{01})k^2 + (a_{10}b_{01} - a_{01}b_{10}).$$

For instability, we must have either $T(k^2) > 0$ or $H(k^2) < 0$ hold for some k. We observe that $T(k^2) < 0$ holds for all k since $a_{10} + b_{01} < 0$. Hence, the condition for Turing instability is $H(k^2) < 0$ for some k. The minimum value of $H(k^2)$ is

$$H_{min} = (a_{10}b_{01} - a_{01}b_{10}) - \frac{(da_{10} + b_{01})^2}{4d}.$$

Hence, we must have $H_{min} = 0$ at the Turing bifurcation threshold and the corresponding critical value of d is given by

$$d_c = \frac{-(2a_{01}b_{10} - a_{10}b_{01}) + \sqrt{(2a_{01}b_{01} - a_{10}b_{01})^2 - a_{10}^2 b_{01}^2}}{a_{10}^2}.$$

For $d > d_c$, the system (5.1) shows non-homogeneous stationary pattern of certain mode under spatially heterogeneous perturbation.

5.5. **Mode Selection**

Suppose that for $d > d_c$, there exists some $k \in (k_{_L}, k_{_R})$ such that $H(k^2) < 0$, where

$$k_{_L}^2 = \frac{(da_{10} + b_{01}) - \sqrt{(da_{10} + b_{01})^2 - 4d(a_{10}b_{01} - a_{01}b_{10})}}{2d}$$

and

$$k_{_R}^2 = \frac{(da_{10} + b_{01}) + \sqrt{(da_{10} + b_{01})^2 - 4d(a_{10}b_{01} - a_{01}b_{10})}}{2d}.$$

Note that $k_{_L}^2$ and $k_{_R}^2$ are obtained from solving $H(k^2) = 0$. If we take $\Omega = [0, L]$, then the n-th mode wave number is $k_n = n\pi/L$. If k_n lies between $k_{_L}$ and $k_{_R}$, then it is an unstable mode and the system (5.1) can show n-th mode pattern solution. This n-th mode selecting bifurcation threshold value is given by

$$M_n: \quad d_c^{(n)} = \frac{b_{01}k_n^2 - det(J)}{k_n^4 - a_{10}k_n^2}. \tag{5.17}$$

Considering η as a bifurcation parameter, we find the corresponding value of $d_c^{(n)}$ and denote this n-th mode selecting threshold curve [45, 46] by M_n in the $\eta - d$ plane. The region above the M_n curve is unstable with respect to the n-th mode solution (see Fig. 4).

Now we take $d > d_c^{(n)}$ with $d - d_c^{(n)}$ small and investigate the appearance of n-th mode pattern solution of the system (5.1). We also examine the amplitude of the resulting pattern solution.

6. Weakly nonlinear analysis

In this section, we apply weakly nonlinear analysis using multi-scale perturbation method and Fredholm theory to derive amplitude equations [26, 27, 47] for the n-th mode Turing patterns solution arising near the critical bifurcation value ($d = d_c^{(n)}$). First, we expand system (5.1) around $E_*(u_*, v_*)$ using Taylor series expansion upto fifth order:

$$\frac{\partial \tilde{u}}{\partial t} = \frac{\partial^2 \tilde{u}}{\partial x^2} + \sum_{i+j=1}^{5} a_{ij}\tilde{u}^i\tilde{v}^j, \quad \frac{\partial \tilde{v}}{\partial t} = d\frac{\partial^2 \tilde{v}}{\partial x^2} + \sum_{i+j=1}^{5} b_{ij}\tilde{u}^i\tilde{v}^j, \tag{6.1}$$

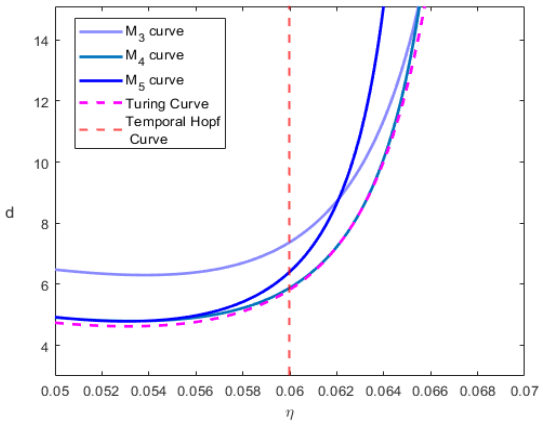

FIGURE 4. Mode curves M_3, M_4 and M_5 in the $\eta - d$ plane. Turing and temporal Hopf curves are also plotted. The domain size $L = 60$ and the other parameters are $a = 0.2, b = 0.15, \alpha = 0.3$.

where

$$\tilde{u} = u - u_*, \tilde{v} = v - v_*,\ a_{ij} = \frac{1}{i!j!}\frac{\partial^{i+j}F_1}{\partial u^i \partial v^j}|_{(u_*,v_*)} \quad \text{and} \quad b_{ij} = \frac{1}{i!j!}\frac{\partial^{i+j}F_2}{\partial u^i \partial v^j}|_{(u_*,v_*)} \quad \text{for } i,j \geq 0.$$

Dropping the tilde for convenience, we write (6.1) in matrix form as

$$\frac{\partial \boldsymbol{U}}{\partial t} = \mathcal{L}\boldsymbol{U} + \boldsymbol{S}, \tag{6.2}$$

where $\boldsymbol{U} = (u, v)^T$, $\mathcal{L} = \begin{pmatrix} a_{10} + \partial_{xx} & a_{01} \\ b_{10} & b_{01} + d\partial_{xx} \end{pmatrix}$ and $\boldsymbol{S} = \begin{pmatrix} \sum_{i+j=2}^{5} a_{ij} u^i v^j \\ \sum_{i+j=2}^{5} b_{ij} u^i v^j \end{pmatrix}$.

Near the mode selecting threshold ($d = d_c^{(n)}$), the evolution of pattern amplitude changes slowly. Thus to capture the amplitude correspond to n-th mode wavenumber, we introduce slow temporal multiple scale

$$t = t(T_1, T_2, T_3, \cdots), \quad \text{where } T_1 = \epsilon t,\ T_2 = \epsilon^2 t,\ T_3 = \epsilon^3 t, \cdots$$

where ϵ is the small perturbation parameter that measures the distance between bifurcation parameter d and the bifurcation threshold ($d = d_c^{(n)}$), i.e.,

$$d = d_c^{(n)} + \epsilon d_1 + \epsilon^2 d_2 + \epsilon^3 d_3 + \epsilon^4 d_4 + \epsilon^5 d_5 + \mathcal{O}(\epsilon^6).$$

The solution of the system (6.2) is also expanded in terms of ϵ:

$$\boldsymbol{U} = \epsilon \boldsymbol{P}_1 + \epsilon^2 \boldsymbol{P}_2 + \epsilon^3 \boldsymbol{P}_3 + \epsilon^4 \boldsymbol{P}_4 + \epsilon^5 \boldsymbol{P}_5 + \mathcal{O}(\epsilon^6),$$

where $\boldsymbol{P}_j = (u_j, v_j)^T$.

These lead to

$$\frac{\partial \boldsymbol{U}}{\partial t} = \epsilon \frac{\partial \boldsymbol{U}}{\partial T_1} + \epsilon^2 \frac{\partial \boldsymbol{U}}{\partial T_2} + \epsilon^3 \frac{\partial \boldsymbol{U}}{\partial T_3} + \epsilon^4 \frac{\partial \boldsymbol{U}}{\partial T_4} + \epsilon^5 \frac{\partial \boldsymbol{U}}{\partial T_5} + \mathcal{O}(\epsilon^6), \quad \boldsymbol{S} = \epsilon^2 \boldsymbol{s}_2 + \epsilon^3 \boldsymbol{s}_3 + \epsilon^4 \boldsymbol{s}_4 + \epsilon^5 \boldsymbol{s}_5,$$

where $\boldsymbol{s}_i$ is the coefficient of ϵ^i in the expansion of the nonlinear term. Further, $\mathcal{L} = \mathcal{L}_c + (d - d_c^{(n)})M$, where

$$\mathcal{L}_c = \begin{pmatrix} a_{10} + \partial_{xx} & a_{01} \\ b_{10} & b_{01} + d_c^{(n)}\partial_{xx} \end{pmatrix} \quad \text{and} \quad M = \begin{pmatrix} 0 & 0 \\ 0 & \partial_{xx} \end{pmatrix}.$$

Substituting these expression into equation (6.2) and equating like power of ϵ, we obtain:

$$O(\epsilon): \quad \mathcal{L}_c \boldsymbol{P}_1 = 0, \tag{6.3}$$
$$O(\epsilon)^2: \quad \mathcal{L}_c \boldsymbol{P}_2 = \boldsymbol{F}, \tag{6.4}$$
$$O(\epsilon^3): \quad \mathcal{L}_c \boldsymbol{P}_3 = \boldsymbol{G}, \tag{6.5}$$
$$O(\epsilon^4): \quad \mathcal{L}_c \boldsymbol{P}_4 = \boldsymbol{H}, \tag{6.6}$$
$$O(\epsilon^5): \quad \mathcal{L}_c \boldsymbol{P}_5 = \boldsymbol{I}, \tag{6.7}$$

where the expressions for $\boldsymbol{F}$, $\boldsymbol{G}$, $\boldsymbol{H}$ and $\boldsymbol{I}$ are given in Appendix B.

Solution of (6.3) under Neumann boundary condition is

$$\boldsymbol{P}_1(x) = \Phi A \cos(k_n x), \tag{6.8}$$

where

$$\Phi = \begin{pmatrix} 1 \\ f \end{pmatrix} \in Ker \begin{pmatrix} a_{10} - k_n^2 & a_{01} \\ b_{10} & b_{01} - d_c^{(n)} k_n^2 \end{pmatrix}, \quad \text{with} \quad f = \frac{k_n^2 - a_{10}}{a_{01}},$$

and A is the amplitude of the pattern which is still unknown at this stage.

Now substitution (6.8) into (6.4) gives rise to a non-homogeneous system. For the solution of such a non-homogeneous system to exist, the right hand side must be orthogonal to the kernel of the adjoint of $\mathcal{L}_c$. This is known as Fredholm solvability condition which imposes $d_1 = 0$ and $T_1 = 0$. Substitution of solution of (6.4) into (6.5) and applying solvability condition again, we obtain Stuart-Landau equation for the amplitude A:

$$\frac{dA}{dt} = \sigma A - l A^3. \tag{6.9}$$

Equation (6.9) is same as the normal form of pitchfork bifurcation. The detailed derivation of (6.9) is given in Appendix B. Note that σ is always positive but the sign of l depends on G_{31} (see Appendix B). We have supercritical case for $l > 0$ and subcritical case for $l < 0$.

6.1. **The supercritical Case**

The system (6.9) has two stable equilibria $A_* = \pm\sqrt{\frac{\sigma}{l}}$ and an unstable equilibrium $A_* = 0$. These stable equilibria are responsible for pattern formation for $d > d_c^{(n)}$ and they attract all non-zero solutions in long time, i.e.,

$$\lim_{t\to\infty} A(t) \equiv A_\infty = \pm\sqrt{\frac{\sigma}{l}}.$$

Hence the solution of (6.2) is given by $\boldsymbol{U} = \sqrt{d - d_c^{(n)}} A_\infty \Phi \cos(k_n x) + \mathcal{O}(\epsilon^2)$ for $d > d_c^{(n)}$. We validate this result in the next section.

6.2. **The subcritical Case**

When $l < 0$, then the system (6.9) has unique equilibrium solution $A = 0$ which cannot represent an amplitude of a pattern. In this case, we need to carry the weakly nonlinear analysis up to $O(\epsilon^5)$. This leads to the following quintic Stuart-Landau equation for the amplitude A (see Appendix C):

$$\frac{dA}{dt} = \tilde{\sigma}A - \tilde{l}A^3 + \tilde{r}A^5, \tag{6.10}$$

where $\tilde{\sigma} = \epsilon^2\hat{\sigma} + \epsilon^4\sigma'$, $\tilde{l} = \epsilon^2\hat{l} + \epsilon^4 l'$ and $\tilde{r} = \epsilon^4 r'$. If $\tilde{\sigma} > 0$, $\tilde{l} < 0$ and $\tilde{r} < 0$ then the equation (6.10) predicts the long-term behavior of the amplitude of the pattern for $d > d_c^{(n)}$ since it admits two stable equilibria $\pm\sqrt{\frac{\tilde{l}-\sqrt{\tilde{l}^2-4\tilde{r}\tilde{\sigma}}}{2\tilde{r}}}$, i.e.,

$$\lim_{t\to\infty} A(t) \equiv A_\infty = \pm\sqrt{\frac{\tilde{l} - \sqrt{\tilde{l}^2 - 4\tilde{r}\tilde{\sigma}}}{2\tilde{r}}}.$$

Hence, the solution of (6.2) is given by $\boldsymbol{U} = \epsilon A_\infty \Phi \cos(k_n x) + \mathcal{O}(\epsilon^2)$ at $d = d_c^{(n)} + d_2\epsilon^2 + d_4\epsilon^4$. Here d_2 and d_4 measure the distance of the bifurcation parameter d from the bifurcation threshold $d_c^{(n)}$ and we choose both as equal to $d_c^{(n)}$. We verify this result too in the next section.

7. Numerical Simulations

We fix temporal parameter values $a = 0.2, b = 0.15$ and $\alpha = 0.3$ and keep the domain size $L = 60$ in all the numerical simulations. We have chosen the initial data to be

$$u(x,0) = u_*\left(1 + \varepsilon\cos\left(\frac{n\pi x}{L}\right)\right) \quad \text{and} \quad v(x,0) = v_*\left(1 + \varepsilon\cos\left(\frac{n\pi x}{L}\right)\right),$$

where $\varepsilon = 10^{-2}$ and n is the desired Turing mode. For $\eta = 0.063$ and $d = 12$, the dispersion relation is shown in Fig. 5. We observe that the largest real part of the growth rate $\lambda(k^2)$ is positive for $k = k_3, k_4$ and k_5 only. We have also plotted the corresponding M_3, M_4 and M_5 mode curves in $\eta - d$ plane together with Turing curve and temporal Hopf curve in Fig. 4. If we decrease η from 0.07 to 0.05 with fixed $d = 12$, then the location of (η, d)

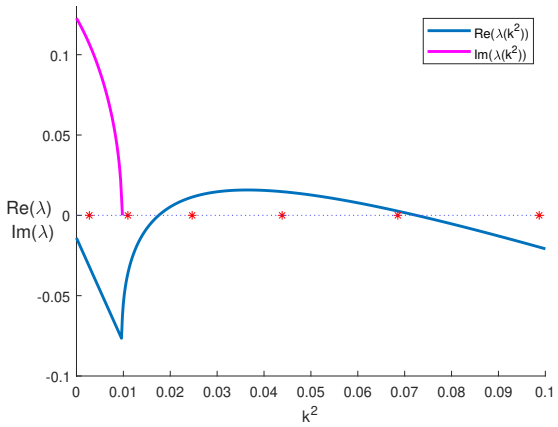

Figure 5. Dispersion relation for $\eta = 0.063$ and $d = 12$. The red points on the horizontal axis correspond to k^2 values for $n = 1, 2, 3, 4, 5$ and 6 modes (from left to right).

moves from stable region to pure Turing region to Turing-Hopf region (see Fig. 4). We plot the corresponding bifurcation diagram (see Fig. 6) in terms of spatial average of u defined by

$$u_{av} = \frac{1}{L}\int_0^L u(x)dx.$$

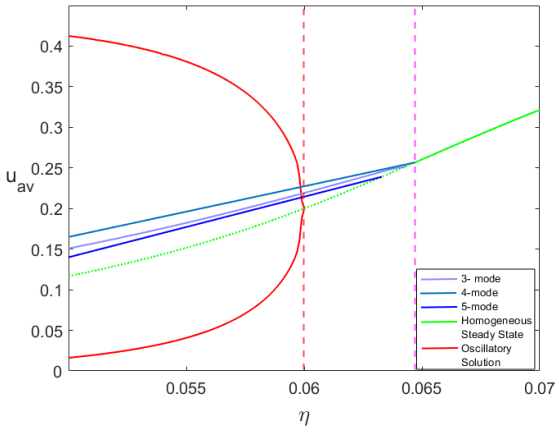

FIGURE 6. Bifurcation diagram for $d = 12$. Here Magenta and red dashed lines represent Turing and temporal Hopf bifurcation thresholds respectively. Other parameter values are $a = 0.2, b = 0.15$ and $\alpha = 0.3$. Refer to text for other details.

In this figure, green color curve represents u_{av} for the homogeneous steady state solution which is stable (solid curve) in the stable region and unstable (dotted curve) otherwise. In the Turing region, Turing pattern solution branches of 3-, 4- and 5- modes emerge from $\eta = 0.0643$, 0.0647 and 0.0633 respectively. Red color curve denotes the oscillatory pattern solution emerging at the temporal Hopf threshold in the Turing-Hopf domain. There exists bistablity between oscillatory solution and non-homogeneous steady state solutions in the Turing-Hopf domain.

Next we consider d as a bifurcation parameter to study the amplitude of Turing pattern in the pure Turing region for fixed $\eta = 0.064$. From (5.17), we see that $d_c^{(3)} = 11.337$ and $d_c^{(4)} = 10.115$ for the 3- mode and 4-mode solutions of the system (5.1). Using weakly nonlinear analysis, we derive the following Stuart-Landau equation of third order for 4- mode solution:

$$\frac{dA}{dt} = \epsilon^2(0.004d_2A - 0.1332A^3). \tag{7.1}$$

The system (7.1) has stable equilibria $A_\infty = \pm 0.1732\sqrt{d_2}$ and the 4- mode pattern solution is stable. Solution u of the system (5.1) using weakly nonlinear analysis at long time t is given by

$$u(x) = u_* + \epsilon A_\infty \cos\left(\frac{4\pi x}{L}\right) = u_* + A_u \cos\left(\frac{4\pi x}{L}\right),$$

where $A_u = \pm 0.1732\sqrt{(d - d_c^{(4)})}$. We compare the numerical solution with that of weakly nonlinear analysis for $d = 10.2$ in Fig. 7 and the two solutions agree well. For 3- mode solution, we find the Stuart-Landau equation at third order as

$$\frac{\partial A}{\partial T_2} = 0.0048d_2A + 1.4435A^3, \tag{7.2}$$

which does not contain any nonzero steady state solution. Hence we carry the weakly nonlinear analysis to $O(\epsilon^5)$ to arrive at

$$\frac{dA}{dt} = \tilde{\sigma}A - \tilde{l}A^3 + \tilde{r}A^5, \tag{7.3}$$

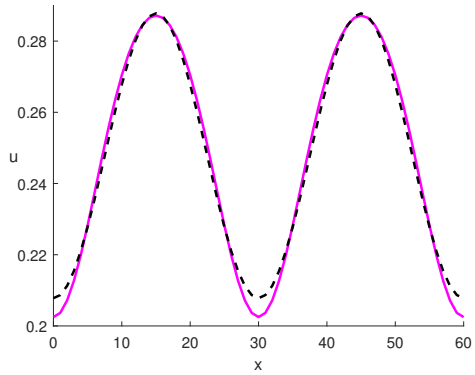

FIGURE 7. Comparison of 4- mode solution of u obtained using weakly nonlinear analysis (black dashed curve) and numerical simulation (magenta color curve). Here parameters values are $d = 10.2$ and $\eta = 0.064$.

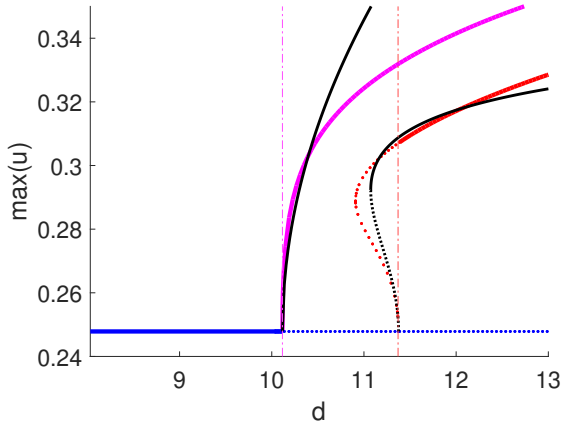

FIGURE 8. Bifurcation diagram in pure Turing domain. Horizontal blue line denotes the homogeneous steady state. Here, red and magenta color curves represent the amplitude of Turing pattern solution, found numerically, for the 3- mode and 4- mode solutions respectively. Black color curves represent the same obtained using weakly nonlinear analysis. Magenta and red vertical lines correspond to the threshold values $d_c^{(4)}$ and $d_c^{(3)}$ respectively. Here temporal parameter values are $a = 0.2$, $b = 0.15$, $\alpha = 0.3$ and $\eta = 0.064$.

where $\tilde{\sigma} = 0.0048d_2\epsilon^2 + (-0.0004d_2^2 + 0.0048d_4)\epsilon^4$, $\tilde{l} = (0.2724\epsilon^2 d_2 - 1.4434)\epsilon^2$ and $\tilde{r} = -388.247\epsilon^4$. The system (7.3) has two stable equilibria

$$A_\infty = \pm\sqrt{\frac{\tilde{l} - \sqrt{\tilde{l}^2 - 4\tilde{r}\tilde{\sigma}}}{2\tilde{r}}},$$

which represent the amplitude of the stable 3- mode Turing solution. Thus, at $d = d_c^{(3)} + \epsilon^2 d_2 + \epsilon^4 d_4$, the maximum of the stable stationary pattern solution is given by $\max(u) = u_* + \epsilon A_\infty$. We have plotted the maximum of u from numerical as well as weakly nonlinear analysis in Fig. 8. For the numerical continuation of stationary solution brunch, we have used pseudo-arc-length continuation method [48, 49]. The system (5.1)

shows homogeneous steady state solution represented by blue solid curve for $d < d_c^{(4)}$. Homogeneous steady solution becomes unstable for $d > d_c^{(4)}$, which is marked by blue dotted line. Magenta color curve represents the 4- mode solution branch emerging at $d = d_c^{(4)}$. We denote 3- mode solution brunch by red color curve appearing at $d = d_c^{(3)}$. And black color curves represent both the 3- and 4- mode solutions from weakly nonlinear analysis. Bistablity between the 3- mode solution and 4- mode solution is observed for $d > d_c^{(3)}$. In this case, the system (5.1) does not exhibit hysteresis since the homogeneous steady-state loses its stability through a super-critical steady-state bifurcation.

In order to obtain hysteresis cycle, we choose $\eta = 0.066$ for which 3-mode curve is nearest to Turing bifurcation curve. The amplitude equation is given by

$$\frac{dA}{dt} = \tilde{\sigma}A - \tilde{l}A^3 + \tilde{r}A^5, \tag{7.4}$$

where $\tilde{\sigma} > 0$, $\tilde{l} < 0$ and $\tilde{r} < 0$.

The stationary solution of the system (7.4) is plotted in Fig. 9a. Homogeneous steady state is stable for $d < d_c^{(3)}$ and otherwise unstable. A pair of unstable backward-bending branches bifurcate from the bifurcation threshold $d = d_c^{(3)}$. These unstable branches change direction and become stable at $d = d_s$. Hence, the system (5.1) has stable 3-mode solutions along with homogeneous stable solution for $d_s < d < d_c^{(3)}$. Different stable states lead to possible hysteresis as the bifurcation parameter d is varied. Based on periodic variation of the bifurcation parameter d shown in Fig. 9a, we demonstrate a hysteresis cycle in Fig. 10. Increasing the parameter d above $d_c^{(3)}$ results in a jump straight to the Turing stable branch, but decreasing d below $d_c^{(3)}$ results in the pattern persisting on the upper stable branch. When d is further decreased below d_s, the solution reaches a homogeneous steady state. In order to form a Turing pattern again, the parameter d must be increased above $d_c^{(3)}$. A comparison between the numerical simulation and analytical results is shown in Fig. 9b. Clearly, the solutions are in agreement near the threshold d_c^3.

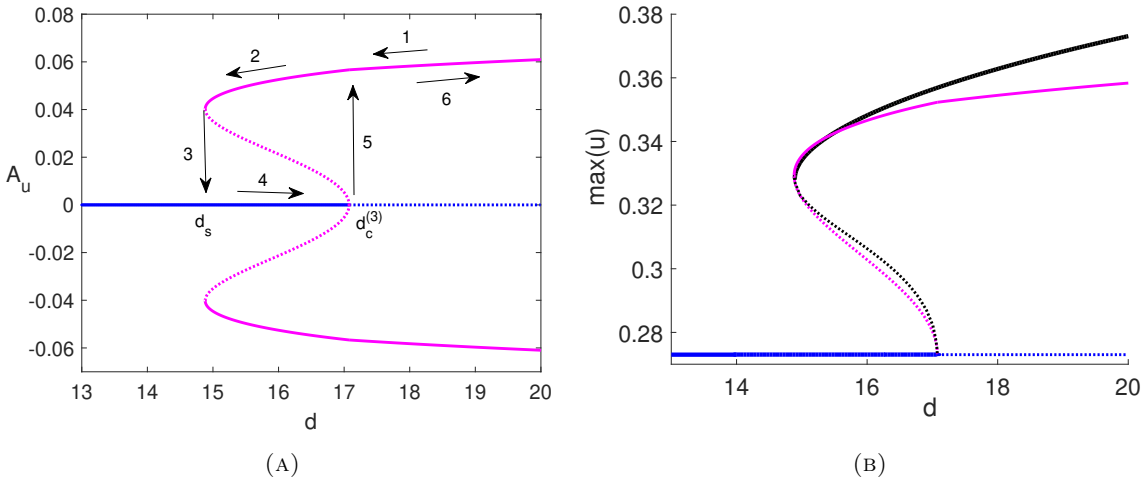

(A) (B)

FIGURE 9. (a) Amplitude of u solution (A_u) from weakly nonlinear analysis for subcritical case. Here $d_c^{(3)} = 17.08$ and $d_s = 14.88$. (b) Comparison of 3- mode solution in maximum of u obtained using weakly nonlinear analysis (magenta color curve) and numerical simulation (black color curve). Other parameter values are $a = 0.2$, $b = 0.15$, $\alpha = 0.3$ and $\eta = 0.066$.

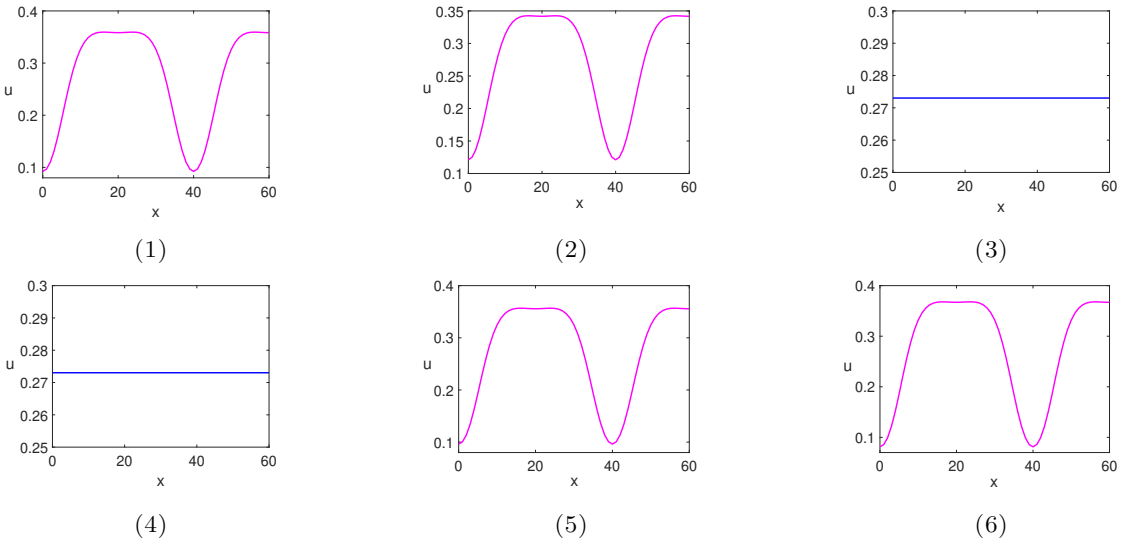

FIGURE 10. A hysteresis cycle corresponds to Fig. (9a). Diffusion parameter d satisfies (1) $d_c^{(3)} < d = 17.5$, (2) $d_s < d = 15.5 < d_c^{(3)}$, (3) $d = 14.8 < d_s$, (4) $d_s < d = 15.5 < d_c^{(3)}$, (5) $d = 17.1 \approx d_c^{(3)}$ (6) $d_c^{3)} < d = 19$.

8. Discussion

Modelling prey-predator interaction and understanding their dynamics have important roles in ecology. Most of the works on prey-predator interaction have been carried out with specialist predators. However, many predators have alternative food resources in addition to the focal prey. Hence, we have considered a prey-predator model with generalist predator and Holling type-II functional response for predation. The temporal and spatio-temporal dynamics under various parametric conditions are investigated. Various complex dynamics such as bistability, tristability, global bifurcations, etc., and their occurrences with parameter values are explored for the temporal model. Most of the literature on spatio-temporal models deal with Turing threshold and the corresponding weakly nonlinear analysis [26–28] around the Turing threshold. In contrast, we have calculated thresholds for various Turing modes and the weakly nonlinear analysis has been carried out around these mode thresholds.

The temporal model exhibits various local bifurcations consisting of saddle-node, transcritical, Hopf, cusp and BT bifurcations. It also shows global bifurcations like homoclinic bifurcation and saddle node bifurcation of limit cycle. Both species persist for $\alpha > a$ either in a co-existing steady state or in an oscillatory state. Note that $\alpha > a$ implies $r_1 b_2 > m r_2$. Thus, persistence of both species can occur when intrinsic growth rate of the prey or intra-species competition in predator become large. It also persists when intrinsic growth rate of predator or consumption rate of prey become small. The prey species go to extinction when parameter values lie in region R_6 for any initial population. The generalist predator population survives due to the availability of alternative food resources. This happens for $\alpha < a$ and $\eta < \eta_{SN_I}$. Since $\eta = r_2/r_1$, the conditions for the existence of predator only population is $r_1 b_2 < m r_2$ and $r_2/r_1 < \eta_{SN_I}$. Combining both we find $b_2/m < r_2/r_1 < \eta_{SN_I}$. Thus, the ratio of intrinsic growth rates of the predator and prey must lie between b_2/m and η_{SN_I} for the predator only population to survive. If we increase the value of η beyond η_{SN_I} keeping $\alpha < a$, then we have a bi-stable region (R_5) in which both the predator only or a co-existing state persist. In terms of dimensional parameters, this bi-stable region exists for $r_2/r_1 > \max\{b_2/m, \eta_{SN_I}\}$. Hence, the bi-stable region consisting of predator only or a co-existing state exists when the intrinsic growth rate of predator far exceeds the intrinsic growth rate of prey. The system (2.2) admits four different types of bistability: (i) one stable axial equilibrium point and a

stable coexistence equilibrium point (region R_5), (ii) two stable coexistence equilibria (region R_3 and R_4), (iii) a stable coexistence equilibrium point and a stable limit cycle enclosing another unstable coexistence equilibrium point (region R_{10}, R_{13} and R_{14}) and (iv) a stable equilibrium point surrounded by an unstable limit cycle which is again enclosed by a stable limit cycle (region R_{11}). For the first three cases, the basins attractions of the attractors are separated by the stable manifold of a saddle coexistence equilibrium point. In the last case, the basins of attraction are separated by an unstable limit cycle. We have also found tri-stability (region R_{12}), where two stable co-existing equilibrium points and a stable limit cycle surrounding them act as attractors. When the system has more than one attractor, the final state of the population species are determined by the initial conditions.

We have also investigated the behaviour of the system in presence of diffusion terms that account for the random movement of the population. We have shown the existence of global solution by showing the boundedness of both the species for all finite time. Also, constructing upper and lower solutions under suitable parametric restriction, we have shown the existence of co-existing non-homogeneous stationary solution. The local stability of the homogeneous steady states have been analyzed with the help of corresponding eigenvalue problems. Further, we have derived the criteria for Turing instability. Further, we have also calculated the threshold values for various Turing mode solutions. The threshold curves representing various unstable Turing modes sometimes cross each other in a two-parametric plane. Also, the unstable Turing mode, which is near the Turing bifurcation threshold, depends on the size of the domain and parameter values. By employing weakly non-linear analysis, we have derived amplitude equation corresponding to n-th unstable mode Turing solution. These solutions corresponding to different modes appear either due to sub-critical or super-critical bifurcation across the mode-thresholds. For sub-critical bifurcation, multiple branches of stable and unstable solutions exist in a range of bifurcation parameter, which may lead to a hysteresis cycle (see Fig. 9a). We have found good agreement between the results of the weakly non-linear analysis and the results of the full numerical solutions of the system (5.1) near the thresholds (see Fig. 8). Multiple stationary Turing patterns corresponding to different unstable modes depend on the choice of initial conditions and these are usually observed in the Turing region. We find the coexistence of stationary and oscillatory solution, depending upon the initial conditions, for parameter values in Turing-hopf domain.

References

[1] A. J. Lotka. Undamped oscillations derived from the law of mass action. *Journal of the American Chemical Society*, 42(8):1595–1599, 1920.

[2] V. Volterra. Variazioni e fluttuazioni del numero d'individui in specie animali conviventi. *C. Ferrari*, 1926.

[3] A. M. Turing. The chemical basis of morphogenesis. *Phil. Trans. Royal Society*, 237:37–72, 1952.

[4] L. A. Segel and J. L. Jackson. Dissipative structure: an explanation and an ecological example. *J. Theor. Biol.*, 37(3):545–59, 1972.

[5] A. Gierer and H. Meinhardt. A theory of biological pattern formation. *Kybernetik*, 12(1), 1972.

[6] S. Kondo and R. Asai. A reaction–diffusion wave on the skin of the marine angelfish pomacanthus. *Nature*, 376:765–768, 1995.

[7] C. A. Klausmeier. Regular and irregular patterns in semiarid vegetation. *Science*, 284:1826–1828, 1999.

[8] A. Marasco, A. Iuorio, F. Cartení, G. Bonanomi, D. M. Tartakovsky, S. Mazzoleni, and F. Giannino. Vegetation pattern formation due to interactions between water availability and toxicity in plant–soil feedback. *Bulletin of mathematical biology*, 76(11):2866–2883, 2014.

[9] A. Medvinsky and S. Petrovskii. Spatiotemporal complexity of plankton and fish dynamics. *SIAM Review*, 44:311–370, 2002.

[10] S. A. Levin and L. A. Segel. Hypothesis for origin of planktonic patchiness. *Nature*, 259(5545):659–659, 1976.

[11] A. Ducrots and M. Langlais. A singular reaction–diffusion system modelling prey–predator interactions: Invasion and co-extinction waves. *Journal of Differential Equations*, 253(2):502–532, 2012.

[12] J. A. Sherratt, B. T. Eagan, and M. A. Lewis. Oscillations and chaos behind predator–prey invasion: mathematical artifact or ecological reality? *Philosophical transactions of the Royal Society of London. Series B: Biological Sciences*, 352(1349):21–38, 1997.

[13] H. Malchow. *Spatiotemporal patterns in ecology and epidemiology: theory, models, and simulation*. Chapman and Hall/CRC, 2007.

[14] J. D. Murray. *Mathematical biology II: spatial models and biomedical applications*, volume 3. Springer New York, 2001.

[15] S. Djilali and S. Bentout. Spatiotemporal patterns in a diffusive predator-prey model with prey social behavior. *Acta Applicandae Mathematicae*, 169(1):125–143, 2020.

[16] E. Venturino and S. Petrovskii. Spatiotemporal behavior of a prey–predator system with a group defense for prey. *Ecological Complexity*, 14:37–47, 2013.
[17] G. F. Gause. *The Struggle for Existence, Williams and Wilkins*. Baltimore, Maryland, 1934.
[18] C. Huffaker. Experimental studies on predation: dispersion factors and predator-prey oscillations. *Hilgardia*, 27(14):343–383, 1958.
[19] W. F. Paquin-Lefebvre, Nagata and M. J. Ward. Pattern formation and oscillatory dynamics in a two-dimensional coupled bulk-surface reaction-diffusion system. *SIAM Journal on Applied Dynamical Systems*, 18(3):1334–1390, 2019.
[20] M. Baurmann, T. Gross, and U. Feudel. Instabilities in spatially extended predator–prey systems: Spatio-temporal patterns in the neighborhood of turing–hopf bifurcations. *Journal of Theoretical Biology*, 245(2):220–229, 2007.
[21] L. Zhang, J. Liu, and M. Banerjee. Hopf and steady state bifurcation analysis in a ratio-dependent predator–prey model. *Commun Nonlinear Sci Numer Simulat*, 44:52–73, 2017.
[22] Z. Ling, L. Zhang, and Z. Lin. Turing pattern formation in a predator–prey system with cross diffusion. *Applied Mathematical Modelling*, 38(21-22):5022–5032, 2014.
[23] M. C. Cross and P. C. Hohenberg. Pattern formation outside of equilibrium. *Reviews of modern physics*, 65(3):851, 1993.
[24] M. Banerjee and S. Petrovskii. Self-organised spatial patterns and chaos in a ratio-dependent predator–prey system. *Theoretical Ecology*, pages 37–53, 2011.
[25] R. Han and B. Dai. Cross-diffusion induced turing instability and amplitude equation for a toxic-phytoplankton–zooplankton model with nonmonotonic functional response. *International Journal of Bifurcation and Chaos*, 27(06):1750088, 2017.
[26] M. Manjun, G. Meiyan, and R. Carretero-González. Pattern formation for a two-dimensional reaction-diffusion model with chemotaxis. *Journal of Mathematical Analysis and Applications*, 475(2):1883–1909, 2019.
[27] B. Bozzini, G. Gambino, D. Lacitignola, S. Lupo, M. Sammartino, and I. Sgura. Weakly nonlinear analysis of turing patterns in a morphochemical model for metal growth. *Computers & Mathematics with Applications*, 70(8):1948–1969, 2015.
[28] M. Banerjee N. Mukherjee, S. Ghorai. Detection of turing patterns in a three species food chain model via amplitude equation. *Communications in Nonlinear Science and Numerical Simulation*, 69:219–236, 2019.
[29] S. V. Petrovskii and H. Malchow. A minimal model of pattern formation in a prey-predator system. *Mathematical and Computer Modelling*, 29(8):49–63, 1999.
[30] I. Boudjema and S. Djilali. Turing-hopf bifurcation in gauss-type model with cross diffusion and its application. *Nonlinear Studies*, 25(3), 2018.
[31] B. I. Camara. Waves analysis and spatiotemporal pattern formation of an ecosystem model. *Nonlinear Analysis: Real World Applications*, 12(5):2511–2528, 2011.
[32] J. Sherratt and S. Matthew. Periodic travelling waves in cyclic populations: field studies and reaction–diffusion models. *J. R. Soc. Interface.*, pages 483–505, 2008.
[33] J. Smoller. *Shock waves and reaction—diffusion equations*, volume 258. Springer Science & Business Media, 2012.
[34] P. D. Spencer and J. S. Collie. A simple predator–prey model of exploited marine fish populations incorporating alternative prey. *ICES Journal of Marine Science*, 53:615–28, 1995.
[35] E. V. Leeuwen, V. A. A. Jansen, and P. W. Bright. How population dynamics shape the functional response in a one-predator–two-prey system. *The Ecological Society of America*, 88(6):1571–1581, 2007.
[36] M. Banerjee and V. Volpert. Spatio-temporal pattern formation in rosenzweig–macarthur model: effect of nonlocal interactions. *Ecological complexity*, 30:2–10, 2017.
[37] M. Baurmann, T. Gross, and U. Feudel. Instabilities in spatially extended predator–prey systems: Spatio-temporal patterns in the neighborhood of turing–hopf bifurcations. *Journal of Theoretical Biology*, 245(2):220–229, 2007.
[38] W. Wang, Q. X. Liu, and Z. Jin. Spatiotemporal complexity of a ratio-dependent predator-prey system. *Physical Review E*, 75(5):051913, 2007.
[39] M. Lio, X. tang, and C. Xu. Stability and instability analysis for a ratio-dependent predator–prey system with diffusion effect. *Nonlinear Analysis: Real World Applications*, 12:1616–1626, 2011.
[40] L. Perko. *Differential Equations and Dynamical Systems*. Springer-Verlag, New York, 2000.
[41] V. Lakshmikantham, S. Leela, and A. A. Martynyuk. *Practical stability of nonlinear systems*. World Scientific, 1990.
[42] M. Giaquinta and G. Modica. Local existence for quasilinear parabolic systems under nonlinear boundary conditions. *Annali di matematica pura ed applicata*, 149(1):41–59, 1987.
[43] W. Walter. Differential inequalities and maximum principles: theory, new methods and applications. *Nonlinear Analysis: Theory, Methods & Applications*, 30(8):4695–4711, 1997.
[44] C. V. Pao. *Nonlinear parabolic and elliptic equations*. Springer Science & Business Media, 2012.
[45] D. Nishiura, Y. Ueyama. A skeleton structure of self-replicating dynamics. *Physica D: Nonlinear Phenomena*, 130(1-2):73–104, 1999.
[46] F. L. Ochoa and J. D. Murray. A non-linear analysis for spatial structure in a reaction-diffusion model. *Bulletin of mathematical biology*, 45(6):917–930, 1983.
[47] R. Han and B. Dai. Cross-diffusion-driven turing instability and weakly nonlinear analysis of turing patterns in a uni-directional consumer-resource system. *Boundary Value Problems*, 2017(1):1–33, 2017.

[48] H. B. Keller. Numerical solution of bifurcation and nonlinear eigenvalue problems. *Application of bifurcation theory*, pages 359–384, 1977.
[49] H. D. Mittelmann. A pseudo-arclength continuation method for nonlinear eigenvalue problems. *SIAM journal on numerical analysis*, 23(5):1007–1016, 1986.

A. Proof of positivity and boundedness

From equation (2.2), we have

$$u(t) = u_0 \ \exp\left[\int_0^t f_1(u(s), v(s))ds\right], \tag{A.1a}$$

$$v(t) = v_0 \ \exp\left[\int_0^t f_2(u(s), v(s))ds\right], \tag{A.1b}$$

which shows that $u(t) \geq 0, v(t) \geq 0$ for all $t \geq 0$ whenever $u_0 \geq 0, v_0 \geq 0$. Hence all solutions starting from non-negative initial conditions remain within the first quadrant of the u-v plane.

To prove the boundedness of the solutions, let us consider two cases: $u_0 \leq 1$ and $u_0 > 1$. For the first case, our claim is that $u(t) \leq 1$ for all $t \geq 0$. If not, let there be t_1, t_2 such that $u(t_1) = 1$ and $u(t) > 1$ for $t_1 < t < t_2$. Then from equation (A.1a), we find

$$\begin{aligned} u(t) &= u_0 \ \exp\left[\int_0^{t_1} f_1(u(s), v(s))ds\right] \ \exp\left[\int_{t_1}^{t_2} f_1(u(s), v(s))ds\right] \\ &= u(t_1) \ \exp\left[\int_{t_1}^{t_2} f_1(u(s), v(s))ds\right] < u(t_1) \qquad t_1 < t < t_2, \end{aligned}$$

since $f_1(u, v) < 0$ for $t_1 < t < t_2$. This contradiction implies that $u(t) \leq 1$ for all $t \geq 0$ whenever $u_0 \leq 1$. For the second case, as long as $u(t) \geq 1$, we have

$$u(t) = u_0 \ \exp\left[\int_0^t f_1(u(s), v(s))ds\right] < u_0.$$

Combining both the cases we have $u(t) \leq \max\{u_0, 1\}$ for all $t \geq 0$. To show the boundedness of v, we consider $X(t) = u(t) + v(t)$. Using (2.2), we find

$$\begin{aligned} \frac{dX}{dt} + X &\leq u(2-u) + v + \eta v(1-v) \qquad (\text{since } b \leq a) \\ &\leq 1 + \frac{(1+\eta)^2}{4\eta} = C \qquad (\text{C is a constant}). \end{aligned}$$

The above inequality leads to $X \leq C - (C - X(0))\exp(-t)$ and hence X remains bounded as $\exp(-t) < 1$ for $t > 0$. Hence $v(t)$ is also bounded. Moreover,

$$\mathcal{A} = \left\{(u, v) \in \mathbb{R}^2_+ : 0 \leq u \leq 1, 0 \leq u + v \leq C\right\}$$

is the positively invariant region for the system (2.2) and all the solutions converge towards the attractor $\mathcal{A}$.

B. Super-critical Amplitude Equation

The non-homogeneous terms used in equation (6.4-6.7) are

$$\begin{aligned}
\boldsymbol{F} &= \frac{\partial \boldsymbol{P}_1}{\partial T_1} - d_1 M \boldsymbol{P}_1 - \boldsymbol{s}_2, \\
\boldsymbol{G} &= \frac{\partial \boldsymbol{P}_1}{\partial T_2} + \frac{\partial \boldsymbol{P}_2}{\partial T_1} - d_1 M \boldsymbol{P}_2 - d_2 M \boldsymbol{P}_1 - \boldsymbol{s}_3 \\
\boldsymbol{H} &= \frac{\partial \boldsymbol{P}_1}{\partial T_3} + \frac{\partial \boldsymbol{P}_2}{\partial T_2} + \frac{\partial \boldsymbol{P}_3}{\partial T_1} - d_1 M \boldsymbol{P}_3 - d_2 M \boldsymbol{P}_2 - d_3 M \boldsymbol{P}_1 - \boldsymbol{s}_4 \\
\boldsymbol{I} &= \frac{\partial \boldsymbol{P}_4}{\partial T_1} + \frac{\partial \boldsymbol{P}_3}{\partial T_2} + \frac{\partial \boldsymbol{P}_2}{\partial T_3} + \frac{\partial \boldsymbol{P}_1}{\partial T_4} - d_1 M \boldsymbol{P}_4 - d_2 M \boldsymbol{P}_3 - d_3 M \boldsymbol{P}_2 - d_4 M \boldsymbol{P}_1 - \boldsymbol{s}_5.
\end{aligned}$$

Using (6.8), we have

$$\boldsymbol{F} = (\boldsymbol{h}_{20} + \boldsymbol{h}_{22}\cos(2k_n x))A^2,$$

where $\boldsymbol{h}_{20} = \boldsymbol{h}_{22} = -\frac{1}{2}\begin{pmatrix} a_{20} + a_{10}f + a_{02}f^2 \\ b_{20} + b_{11}f + b_{02}f^2 \end{pmatrix}$.

Define

$$\mathcal{L}_j = \begin{pmatrix} a_{10} - j^2 k_n^2 & a_{01} \\ b_{10} & b_{01} - j^2 k_n^2 d_c^{(n)} \end{pmatrix} \text{ for } j = 0, 1, 2, 3, 4.$$

Solving (6.4) we have

$$\boldsymbol{P}_2 = (\boldsymbol{k}_{20} + \boldsymbol{k}_{22}\cos(2k_n x))A^2, \tag{B.2}$$

where $\mathcal{L}_0 \boldsymbol{k}_{20} = \boldsymbol{h}_{20}$ and $\mathcal{L}_2 \boldsymbol{k}_{22} = \boldsymbol{h}_{22}$. Let $\boldsymbol{k}_{2i} = \begin{pmatrix} k_{2i}^{[1]} \\ k_{2i}^{[2]} \end{pmatrix}$ for $i = 0, 2$. The kernel of the adjoint of the L_c is given by

$$\bar{\boldsymbol{P}}_1 = \bar{\Phi} A \cos(k_n x),$$

where

$$\bar{\Phi} = \begin{pmatrix} \frac{b_{10}}{k_n^2 - a_{10}} \\ 1 \end{pmatrix} \in Ker \begin{pmatrix} a_{10} - k_n^2 & b_{10} \\ a_{01} & b_{01} - d_c^{(n)} k_n^2 \end{pmatrix}.$$

Using the expression of $\boldsymbol{P}_2$ we have

$$\boldsymbol{G} = \frac{\partial \boldsymbol{P}_1}{\partial T_2} + \boldsymbol{G}_{11} A \cos(k_n x) + \boldsymbol{G}_{31} A^3 \cos(k_n x) + \boldsymbol{G}_{33} A^3 \cos(3k_n x),$$

where

$$\begin{aligned}
\boldsymbol{G}_{11} &= \begin{pmatrix} 0 \\ -d_2 k_n^2 f \end{pmatrix}, \boldsymbol{G}_{33} = -\frac{1}{4}\begin{pmatrix} a_{30} + a_{21}f + a_{12}f^2 + a_{03}f^3 \\ b_{30} + b_{21}f + b_{12}f^2 + b_{03}f^3 \end{pmatrix} \text{ and} \\
\boldsymbol{G}_{31} &= -\begin{pmatrix} k_{22}^{[2]}(\frac{1}{2}a_{11} + a_{02}f) + k_{22}^{[1]}(\frac{1}{2}a_{11}f + a_{20}) + k_{20}^{[2]}(a_{11} + 2a_{02}f) + k_{20}^{[1]}(a_{11}f + 2a_{20}) \\ k_{22}^{[2]}(\frac{1}{2}b_{11} + b_{02}f) + k_{22}^{[1]}(\frac{1}{2}b_{11}f + b_{20}) + k_{20}^{[2]}(b_{11} + 2b_{02}f) + k_{20}^{[1]}(b_{11}f + 2b_{20}) \end{pmatrix} + 3\boldsymbol{G}_{33}.
\end{aligned}$$

Using Fredholm solvability condition in equation (6.5), we obtain

$$\frac{\partial A}{\partial T_2} = \hat{\sigma} A - \hat{l} A^3, \tag{B.4}$$

where

$$\hat{\sigma} = -\frac{< \boldsymbol{G}_{11}, \bar{\Phi} >}{< \Phi, \bar{\Phi} >} \text{ and } \hat{l} = \frac{< \boldsymbol{G}_{31}, \bar{\Phi} >}{< \Phi, \bar{\Phi} >}.$$

Since $\frac{dA}{dt} = \epsilon^2 \frac{\partial A}{\partial T_2}$, we obtain the Stuart-Landau equation as

$$\frac{dA}{dt} = \sigma A - lA^3,$$

where $\sigma = \epsilon^2 \hat{\sigma}$ and $l = \epsilon^2 \hat{l}$.

C. Sub-critical Amplitude Equation

Substituting (B.4) in the expression of $\boldsymbol{G}$, we obtain the solution of (6.5) as

$$\boldsymbol{P}_3 = \boldsymbol{C}_{11} A \cos(k_n x) + \boldsymbol{C}_{31} A^3 \cos(k_n x) + \boldsymbol{C}_{33} A^3 \cos(3k_n x), \tag{C.1}$$

where $\mathcal{L}_1 \boldsymbol{C}_{11} = \boldsymbol{G}_{11} + \hat{\sigma}\Phi$, $\mathcal{L}_1 \boldsymbol{C}_{31} = \boldsymbol{G}_{31} - \hat{l}\Phi$. and $\mathcal{L}_3 \boldsymbol{C}_{33} = \boldsymbol{G}_{33}$. Now from the solvability condition for (6.6), we choose $d_3 = 0$ and $T_3 = 0$ to remove the secular terms. Substituting $\boldsymbol{P}_3$, we get

$$\boldsymbol{H} = \boldsymbol{H}_{20} + \boldsymbol{H}_{22} A^2 \cos(2k_n x) + \boldsymbol{H}_{40} + \boldsymbol{H}_{42} A^4 \cos(2k_n x) + \boldsymbol{H}_{44} A^4 \cos(4k_n x).$$

Further, solving (15) we find

$$\boldsymbol{P}_4 = \boldsymbol{D}_{20} + \boldsymbol{D}_{22} A^2 \cos(2k_n x) + \boldsymbol{D}_{40} + \boldsymbol{D}_{42} A^4 \cos(2k_n x) + \boldsymbol{D}_{44} A^4 \cos(4k_n x), \tag{C.2}$$

where $\mathcal{L}_0 \boldsymbol{D}_{20} = \boldsymbol{H}_{20}$, $\mathcal{L}_0 \boldsymbol{D}_{40} = \boldsymbol{H}_{40}$, $\mathcal{L}_2 \boldsymbol{D}_{22} = \boldsymbol{H}_{22}$, $\mathcal{L}_2 \boldsymbol{D}_{42} = \boldsymbol{H}_{42}$ and $\mathcal{L}_4 \boldsymbol{D}_{44} = \boldsymbol{H}_{44}$. The right hand side of equation (6.7) becomes

$$\boldsymbol{I} = \frac{\partial A}{\partial T_4}\Phi + \boldsymbol{I}_{11} A \cos(k_n x) + \boldsymbol{I}_{31} A^3 \cos(k_n x) + \boldsymbol{I}_{51} A^5 \cos(k_n x) + \boldsymbol{I}^*,$$

where the $\boldsymbol{I}^*$ contains the orthogonal term of $\bar{\boldsymbol{P}}_1$ in $\boldsymbol{I}$. Explicit expressions of $\boldsymbol{H}_{ij}, \boldsymbol{I}_{ij}$ are omitted here for brevity.

Again using Fredholm solvability condition in equation (6.7), we obtain quintic Stuart-Landau equation as

$$\frac{\partial A}{\partial T_4} = \sigma' A - l' A^3 + r' A^5,$$

where

$$\sigma' = -\frac{< \boldsymbol{I}_{11}, \bar{\Phi} >}{< \Phi, \bar{\Phi} >},\ l' = \frac{< \boldsymbol{I}_{31}, \bar{\Phi} >}{< \Phi, \bar{\Phi} >} \text{ and } r' = -\frac{< \boldsymbol{I}_{51}, \bar{\Phi} >}{< \Phi, \bar{\Phi} >}.$$

Since $\frac{dA}{dt} = \epsilon^2 \frac{\partial A}{\partial T_2} + \epsilon^4 \frac{\partial A}{\partial T_4}$, we finally obtain

$$\frac{dA}{dt} = \tilde{\sigma} A - \tilde{l} A^3 + \tilde{r} A^5, \tag{C.3}$$

where $\tilde{\sigma} = \epsilon^2 \hat{\sigma} + \epsilon^4 \sigma'$, $\tilde{l} = \epsilon^2 \hat{l} + \epsilon^4 l'$ and $\tilde{r} = \epsilon^4 r'$.